ACS Catalysis

pubs.acs.org/acscatalysis Research Article

Versatile and Robust Nickel Single Atom Catalysts

Brandon Burnside, Jesse Larence, Ryan Alcala, Stephen Porter, Andrew DeLaRiva, Karl Kharas, Christopher Riley,[1] Angelica Benavidez, Nicholas Jaegers, Geunho Han, Justin Notestein, Siddhant Singh, Robert W.J. Scott, Lulu Chen, Juan Li, Sen Lin, Hua Guo, Shan Jiang, Wei-Ling Huang, Jeffrey T. Miller, and Abhaya K. Datye*

Cite This: *ACS Catal.* 2026, 16, 10207−10221 Read Online

ACCESS | Metrics & More | Article Recommendations | Supporting Information

ABSTRACT: A vast number of industrial catalytic processes rely on noble metals, also called platinum group metals (PGMs), which are scarce and expensive. Replacing these expensive noble metals with Earth abundant metals represents a major challenge. Although nickel is known to be an effective catalyst for certain reactions, like hydrogenation, it is unselective in metallic form and is inactive when oxidized. Here, we show that many of the reactions catalyzed by PGMs, such as oxidation or hydrogenation, can also be carried out by a base metal such as nickel, when it is stabilized in the form of isolated single atoms in square planar coordination within the fluorite lattice of CeO_2. Incorporating Ni into the CeO_2 lattice ($Ce_{0.9}Ni_{0.1}O_{2-x}$) creates a versatile and robust Ni single atom catalyst. The working catalyst contains atomically dispersed Ni^{2+} sites that are stable under reaction conditions. Unlike metallic Ni, this single atom catalyst is not pyrophoric, can be handled in air, and easily activated for hydrogenation reactions. The synthesis described here is scalable and yields a high loading of Ni (~3 wt %) within the fluorite CeO_2 lattice while also allowing facile substitution of Ce with co-dopants, such as Zr, to further tune the environment of the active sites.

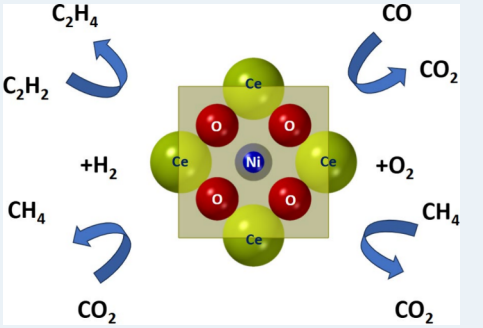

KEYWORDS: *single atom nickel catalyst, selective acetylene hydrogenation, methane oxidation, CO oxidation, Earth abundant catalyst*

INTRODUCTION

Single atom catalysts (SAC)[1] have captured the community's interest over the past decade. While these catalysts allow for maximum atom efficiency, their broader application in industry is hindered by lack of stability, because the single atom species are prone to sintering into nanoparticles with diminished performance.[2] One strategy to improve stability is to isolate the single atom species by depositing on average only one active metal atom on each crystallite of support, so the metal species cannot aggregate to form clusters and nanoparticles. However, this approach is only possible with very low loading of the active phase.[3] If the single atom species are strongly bonded to the support through atom trapping, it is possible to ensure thermal stability, at elevated temperatures.[4] However, SACs prepared in this manner generally show low catalytic activity because the metal atoms are fully coordinated (e.g., four-fold coordination of Pt on cerium oxide-ceria).[5] The thermally stable single atoms must be first converted into metallic nano particles to achieve high reactivity.[6] Here we show that single atoms of Ni coordinated to ceria as 16-electron complexes can be surprisingly active for reactions involving oxygen as well as hydrogen, without a need to convert them into metallic Ni.

In the literature, nickel SACs have been prepared on a wide range of supports, including N-doped carbon nanotubes, carbon nitride, graphene, on metal nanoparticles such as Au, Cu, and Pt in the form of single atom alloys, and on metal oxides such as MgO, CeO_2, and Y_2O_3.[7−9] The most common application for nickel SACs has been in electrocatalytic reactions such as CO_2 reduction,[10−12] ORR (oxygen reduction reaction),[13] and OER (oxygen evolution reaction).[14−16] Reports of nickel SACs for thermal catalysis are generally limited to zeolites, where ionic Ni is exchanged into extra framework sites.[17−19] On oxide supports, it is necessary to convert ionic Ni to the metallic form to make it active. For example, when Ni is incorporated into the spinel ($NiAl_2O_4$)[20,21] or in a perovskite,[22,23] the Ni is octahedrally coordinated and strongly bound, achieving high thermal stability. But the nickel is not active for hydrogenation, or reforming, unless it is reduced to form metallic Ni via exsolution.[24] In the present work, we show that on a ceria support, nickel single atoms in oxidized form result in a catalyst with excellent reactivity for a range of reactions which are not

Received: February 5, 2026
Revised: April 17, 2026
Accepted: April 20, 2026
Published: April 30, 2026

https://doi.org/10.1021/acscatal.6c00872
ACS Catal. 2026, 16, 10207−10221

known to occur on Ni^{2+}. Since the catalyst contains oxidized nickel, it can also be easily handled in air, with no need for passivation, hence it is not pyrophoric, which otherwise makes handling metallic Ni catalysts more difficult.

This work highlights the stability and versatility of atomically dispersed ionic nickel when present in a fluorite ceria lattice. The ionic nickel catalyst was synthesized with a solgel technique to create a Ni doped ceria (single phase fluorite structure). The high nickel loading sample which will be referred to as $Ni_{0.1}Ce_{0.9}O_{2-x}$ (~3.4 wt % Ni) allowed the use of characterization techniques such as XAS, XRD, pair distribution function (PDF), XPS, and DRIFTS and catalytic testing over a range of reactions and environments. Under reducing conditions where hydrogenation of CO_2 and C_2H_2 was investigated, the ionic nickel shows much higher levels of selectivity compared with metallic nickel. Under oxidizing conditions where the highly exothermic oxidation reactions of CO and CH_4 oxidation were studied, the Ni^{2+} outperforms widely used catalysts such as Pt, due to the lack of poisoning by CO, and limited impact of H_2O. In each case, the catalysts were characterized post-reaction to ensure that the active phase contained Ni^{2+} species only. The results presented here are surprising, since Ni^{2+} ions dispersed within oxides, such as NiO, or in spinel or perovskite structures, do not catalyze hydrogenation or oxidation reactions. It is evident that CeO_2 as a support plays a significant role.[25,26] While CeO_2 by itself is also active for these reactions,[27−29] its activity is very low, except for methane oxidation. Even for methane oxidation, we show that the Ni SAC catalyst in ceria is intriguingly more active than ceria alone. CeO_2 is known to be an oxygen transfer catalyst in emission control catalysts, but its role in hydrogenation reactions is not well understood. As we show in this work, the performance of Ni^{2+} for oxidation and hydrogenation reactions can be related to its square planar, 4-fold coordination observed in ceria, unlike other oxides where the Ni^{2+} shows tetrahedral or octahedral coordination. We present a detailed analysis of the structure of these catalysts, before and after reaction, demonstrating that single atom Ni in ceria represents a robust and versatile catalyst.

Materials

Chemicals used in the synthesis; $Ce(NO_3)_2$* $6H_2O$, $Al(NO_3)_3$ * $9H_2O$, (99.999% trace metal basis) used as received from Sigma-Aldrich. $Ni(NO_3)_2$ * $6H_2O$ (99.998% trace metal basis) used as received from Alfa-Aesar. Deionized water was used throughout the study. Methane (UHP), nitrogen (UHP), CO_2 (research grade) from Airgas were used in reactivity experiments without further purification. Argon (UHP), 10% H_2/Ar (UHP), nitrogen (UHP), and Oxygen (UHP) from Airgas were used in the temperature-programmed reduction (TPR).

Methods

PVP Sol-Gel Synthesis. The nickel SACs were prepared using nickel nitrate and cerium nitrate precursors via a sol-gel synthesis route described previously.[30] By using a polymeric complexing agent, poly vinyl pyrrolidone (PVP), we ensure intimate mixing between the Ni and Ce cations, preventing precipitation and segregation of the components. All catalysts were calcined in flowing air at 500 °C for 2 h to remove organic precursors and the nitrate species, yielding atomically dispersed Ni uniformly distributed in the ceria support. This method allows us to prepare catalysts where nickel is atomically dispersed throughout the bulk of the ceria. The nominal composition of the catalysts was $Ce_{0.9}Ni_{0.1}O_{2-x}$. The synthesis is flexible and allows addition of co-dopants, which we illustrate with the sample $Ce_{0.9}Ni_{0.05}Zr_{0.05}O_{2-x}$. The method of preparation is also conducive to the synthesis of high entropy oxides, which show enhanced performance for reactions such as dry reforming of methane.[20] All the samples were calcined at 500 °C for 2 h by heating at a ramp rate of 1 °C/min.

Ni Catalysts via Incipient Wetness Impregnation. A reference catalyst was prepared using nickel nitrate and polyhedral ceria (ceria prepared by decomposition of Ce nitrate at 380 °C in air for 5 h). Nickel nitrate was dissolved in 15 ml to get 3 wt % nickel and deposited onto the CeO_2 support then dried at 100 °C for 24 h. After which, the sample was calcined at 500 °C for 2 h. The sample was then reduced in H_2 at 500 °C for 30 min and passivated at room temperature with pulses of 10% O_2/He. A similar synthesis procedure was used for the silica and alumina-supported Ni reference catalysts.

XRD. X-ray diffraction (XRD) measurements were conducted on a Rigaku SmartLab with the 2 Theta from 15° and 85°, using a scanning rate of 1°/min at a step of 0.01°. The radiation used was Cu K-α and also Co K-α. Synchrotron powder XRD was also performed at the Canadian Light Source as described in more detail in the Supporting Information.

XRF. The analysis was performed using an Orbis Micro-XRF Analyzer, an energy dispersive spectrometer, operated in vacuum with a Rh source and a 30mm^2 silicon drift detector. The instrument settings included a voltage of 25 kV and a current range of 800−900 μA, maintaining a dead time between 30−50%, which is optimal for accurate measurements. A consistent 2 mm spot size and a working distance of approximately 77 mm were used to ensure uniform analysis across measurements. Each sample was analyzed at five different areas to ensure representative sampling and to assess sample homogeneity, yielding $Ce_{0.9}Ni_{0.1}O_{2-x}$ ~ 3.4 wt % Ni, Ni/SiO_2 ~ 3.1 wt % Ni.

Temperature-Programed Reduction. TPR experiments were carried out on a Micromeritics AutoChem II 2920 instrument equipped with a cold trap and a TCD detector. The samples were diluted to account for the varying loading of nickel. For the TPR experiments, an initial oxidative pretreatment was performed where the samples were heated to 300 °C at a rate of 50 °C/min under 10% O_2/He and held for 1 h. To remove any surface adsorbates that may have been on the as-prepared catalyst. After which the system was flushed with Argon while the sample was returned to room temperature. Subsequently, the carrier gas was changed to 10% H_2/Ar and the sample temperature was ramped from 35 to 800 °C at a rate of 10 °C/min.

CO-DRIFTS. Diffuse reflectance infrared Fourier transform spectroscopy (DRIFTS) with a probe molecule of carbon monoxide (CO) was conducted by a Thermo Nicolet 6700 FTIR spectrometer equipped with a praying mantis diffuse reflectance sample holder in the REACT core facility at Northwestern University. Samples were loaded inside the sample holder without dilution. Each sample went through a series of pairs of pretreatment and CO DRIFTS. The pretreatments were (1) 350 °C for 1 h with 10% O_2 in Ar, (2) 250 °C for 1 h with 5% H_2 in Ar, (3) 500 °C for 1 h with 5% H_2 in Ar, and (4) 450 °C 1 h with 5% CO in Ar. After each pretreatment, the holder was purged with He until the holder temperature was cooled to 40 °C. Then, the background spectrum was obtained, and the CO/Ar gas flowed into the sample holder until the sample was saturated with CO molecules. After removing the remaining CO molecules with Ar, the CO vibrational bands on the sample surface were obtained by subtracting the background.

https://doi.org/10.1021/acscatal.6c00872
ACS Catal. 2026, 16, 10207−10221

The diffuse reflectance spectra were acquired by the average of 256 scans with a resolution of 4 cm^{-1} and then the Kubelka-Munk transform ($KM = (1 - R)^2/2R$, where R is reflectance) with the OMNIC FTIR software (Thermo Scientific) was applied to the spectra.

TEM. Samples were dispersed in ethanol and mounted on holey carbon grids for examination in the JEOL NeoARM 200CF transmission electron microscope equipped with a spherical aberration corrector to allow atomic resolution imaging and an Oxford Aztec Energy Dispersive System (EDS) for elemental analysis. The microscope is equipped with two large area JEOL EDS detectors for higher throughput in the acquisition of X-ray fluorescence signals. Images were recorded in annular dark field (ADF) mode and in annular bright field (ABF) mode.

Activity Measurements. Acetylene selective hydrogenation: 47 mg of catalyst were mixed with 47 mg of extra- coarse silicon carbide and loaded into a quartz tube 4 mm ID, with quartz wool plugs. A gas mixture of C_2H_2:C_2H_4:H_2:N_2 (1:76:4:129) with a GHSV of 32.55 ($L/g_{cat}h$) was used and the products analyzed by gas chromatography with an Agilent 6890 with FID detector and a GS-alumina PLOT column.

Ethylene hydrogenation: 50 mg of each sample (Ni/Al_2O_3 and $Ce_{0.9}Ni_{0.1}O_{2-x}$) was tested for ethylene hydrogenation. 25 mL/min of 2% ethylene in N_2, 2 mL/min of pure H_2) were reacted at 75 °C for 30-minute periods after being subjected to the following treatments (a) after a reduction in 4% H_2 for 1 h at 350 °C (b) after acetylene hydrogenation for 30 min (25 mL/min of 2% acetylene and 2 mL/min of H_2) and (c) after oxidation in air for 1 h at 350 °C.

CO oxidation: Catalysts were tested and compared using CO oxidation as a reaction probe. 20 mg of catalyst was loaded between quartz wool in a quartz tube reactor. A feed gas consisting of 1.5 mL/min CO, 1 mL/min O_2 and 75 mL/min He was used, giving a total space velocity of 232,500 mL $g^{-1}h^{-1}$. The temperature of the reactor was raised to a maximum of 300 °C at a heating rate of 2 °C/min. Three consecutive runs were performed on each sample and data from the third run was plotted herein. A Varian CP-4900 micro gas chromatograph equipped with two channels was used to analyze gas composition.

CH_4 oxidation: 30 mg of catalyst were mixed with 30 mg extra coarse silica carbide. Loaded into a quartz tube 4 mm ID, with quartz wool plugs. A gas mixture of CH_4:O_2:N_2 (1:4:20) with a total flow of 30 mL/min. Giving a GHSV of 60 ($L/g_{cat}h$). The samples were then heated at 1 °C/min.

CO_2 hydrogenation: 30 mg of catalyst were mixed with 30 mg extra coarse silica carbide. Loaded into a quartz tube 4 mm ID, with quartz wool plugs. A gas mixture of CO_2:H_2:N_2 (1:3:4) with a total flow of 24 mL/min. Giving a GHSV of 48 ($L/g_{cat}h$). The samples were then heated at 1 °C/min. Only the Ni/SiO_2 sample was pretreated with H_2 at 500 °C before the trial, the other samples were not given any pretreatments.

CH_4 oxidation and CO_2 hydrogenation activity were measured using an Agilent 4 column 490 MicroGC. 3 columns were used to measure the gases. Hydrogen and Nitrogen were measured on a 10 m MS5A column with Argon as the carrier gas. CO was measured on a 10 m MS5A column with Helium as the carrier gas. CO_2 and CH_4 were measured on a 10 m PPU (PoraPlot U) column with Helium as the carrier gas.

Experimental Details at NSLS-II. Ni K edge XAS were conducted at the Brookhaven National Laboratory (BNL) National Synchrotron Light Source II (NSLS-II) 8-ID ISS beamline. For the in-situ experiment, the samples were ground and sieved into fine powder and loaded into the capillary tube. The tube is assembled on the in-situ cell and sealed with epoxy glue. The thermocouple was inserted into the sample bed, and two heating coils were placed on the sides of tube to control the temperature. A Ni foil spectrum was simultaneously obtained with the sample for energy calibration.

WinXAS was used to fit the data. The XANES were normalized with linear and third order polynomials in the pre-edge and post-edge regions, respectively. WinXAS was used to fit first shell peaks in the k^2 weighted Fourier transform of the EXAS data from k = 2.5−9.9 $Å^{-1}$. Ni foil with 12 Ni−Ni bonds at 2.49 Å was fit to determine So, which was 0.80. Optimization of sigma-squared was obtained from fitting the isolated peaks in k-space.

Additional experimental details for the Canadian Light Source are included in the Supporting Information.

Nuclear Magnetic Resonance. Magnetic resonance measurements were preceded by catalyst treatment at 423 K for 3 h in high-vacuum (∼10−5 mbar) to remove water. The treated samples were then packed inside an argon-filled Schlenk flask until they were removed and loaded into 4.0 mm pencil-type Bruker NMR rotors. 1H MAS NMR experiments were conducted with a 11.7434 T Bruker 500WB spectrometer utilizing a commercial 4.0x mm pencil-type HX MAS probe and a spinning rate of 8 kHz. The corresponding 1H Larmor frequency is 500.1330008 MHz. Single pulse NMR experiments were conducted with a π/4 pulse width of 5 μs, a delay time of 5 or 0.5 s, a spectral width of 0.1 MHz, and an acquisition time of 0.163 s. Typically, 32 scans were collected for each NMR spectrum. Chemical shifts were externally referenced to the center band of adamantane at 1.82 ppm.

DFT Methods. The model for Ni-doped $CeO_2(111)$ surface consists of repeating supercells each with 144 atoms in 3 layers. The slabs are separated by a 15 Å vacuum along the z-axis to eliminate periodic interactions. The bottom O−Ce−O trilayer was held fixed to emulate bulk-like behavior while allowing the upper layers and adsorbates to relax completely.

Spin-polarized density functional theory (DFT) calculations were conducted using the Vienna Ab Initio Simulation Package (VASP), employing the Perdew-Burke-Ernzerhof (PBE) generalized gradient approximation (GGA) for the exchange-correlation functional. The projector augmented wave (PAW) method was used to treat electron-ion interactions, with a plane-wave basis set cutoff energy of 400 eV. To address the strong correlation effects in Ce 4f electrons, a Hubbard U correction was applied with an effective U parameter (Ueff) of 4.5 eV, consistent with literature values for accurate description of electron localization upon oxygen vacancy formation. Occupation numbers were smeared using the Gaussian method with a width of 0.05 eV. Structural relaxations were carried out until atomic forces converged below 0.05 eV/Å, and van der Waals interactions were incorporated via the DFT-D3 method with Becke-Johnson damping. Brillouin zone sampling was restricted to the Γ-point for all calculations. The bulk lattice parameter of CeO_2 optimized to 5.47 Å, in good agreement with experimental values (∼5.41 Å).

Reaction energy barriers were determined using the climbing-image nudged elastic band (CI-NEB) method, followed by quasi-Newton refinement. First-order saddle points were confirmed by the presence of a single imaginary frequency for transition state in vibrational frequency analysis.

https://doi.org/10.1021/acscatal.6c00872
ACS Catal. 2026, 16, 10207−10221

RESULTS

Characterization of the As-Prepared Catalyst

XRD patterns (Figure 1a) of the nickel doped ceria catalyst show only the ceria crystal lattice reflections. All peaks are indexed to the ceria fluorite structure (*Fm3m*) with the CeO_2 lattice reflections indicated by diamonds. The XRD peaks were fitted using JADE software that allowed identification of the phases present in the calcined sample. Figure S1a and Figure S1b in the Supporting Information show the fits to the XRD data for $Ce_{0.9}Ni_{0.1}O_{2-x}$ and $Ce_{0.9}Ni_{0.05}Zr_{0.05}O_{2-x}$ and the absence of any crystalline phases associated with nickel or zirconium. The inclusion of zirconium as a dopant cation has been shown in previous studies to stabilize ceria surface area at high temperatures.[31−33]

The inclusion of smaller isovalent cations creates a defective face centered cubic (fcc) fluorite structure with increased oxygen mobility. The lattice constants (Table S1) obtained by the JADE software fit (Figure S1a and S1b) show a decrease in the lattice constant from 5.410 Å for pure ceria to 5.408 Å for the 10 mol% Ni doped in ceria, consistent with the literature.[34] Since no internal standards were used for the XRD, the variations in the lattice constant are within experimental error and cannot be directly related to the presence of the dopant. TEM images of the $Ce_{0.9}Ni_{0.1}O_{2-x}$ sample along with EDS maps shown in Figure 1b suggest that the Ni is uniformly distributed in this sample. A reference sample containing a similar weight loading (3 wt %) of Ni/SiO_2 was prepared to contrast the physical characteristics and reactivity with the SAC, as

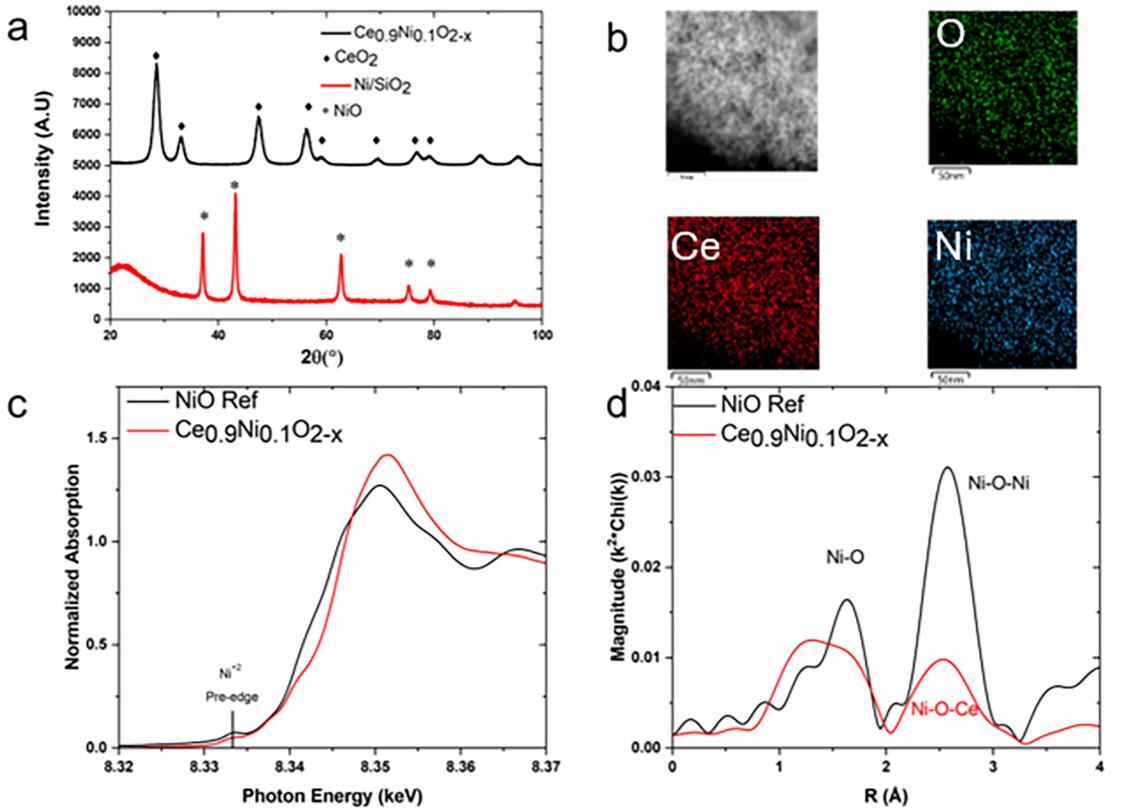

e

Sample	Scatter	CN	R, Å
$Ce_{0.9}Ni_{0.1}O_x$	Ni-O	3.6	1.92
	Ni-O-Ce	2.4	3.08
NiO	Ni-O	6.0	2.09
	Ni-O-Ni	12.0	2.96

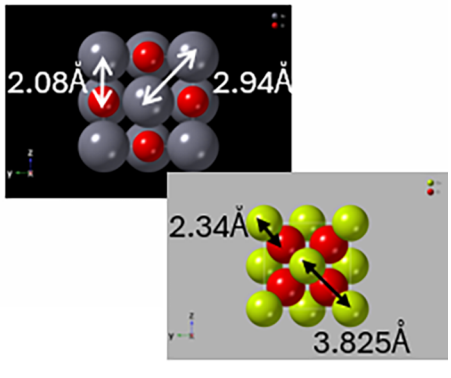

Figure 1. (a) XRD pattern of the as-prepared $Ce_{0.9}Ni_{0.1}O_{2-x}$ and Ni/SiO_2 samples. (b) STEM imaging of the as-prepared $Ce_{0.9}Ni_{0.1}O_{2-x}$ sample with EDS mapping of Ce (red), Ni (blue), and O (green). (c) Ni K-edge XANES of as-prepared samples $Ce_{0.9}Ni_{0.1}O_{2-x}$ (red) and NiO (black). (d) FT of k^2-weighted EXAFS from 2.5 to 10.1 $Å^{-1}$. (e) Table of EXAFS fits for the as-prepared samples. (f) Model of CeO_2 and NiO with the bond distances of the first and second nearest neighbors labeled (O: red, Ni: gray, and Ce: green).

https://doi.org/10.1021/acscatal.6c00872
ACS Catal. 2026, 16, 10207−10221

shown via XRD (Figure 1a) and HRTEM (Figure S2). Particles of NiO are seen in the HRTEM image and the XRD pattern shows peaks corresponding to bulk NiO that are not seen for the SAC. Nunan and Bortun,[33] reported similar observations for ceria-zirconia containing trivalent rare earths and a number of transition metals, including Ni.

The $Ce_{0.9}Ni_{0.1}O_{2-x}$ sample was analyzed at beamline ID-8 at NSLS-II using x-ray absorption spectroscopy (XAS). Details on the experimental set up and acquisition parameters are provided in the Supporting Information. The XANES and EXAFS regions of the data for the bulk NiO and the $Ce_{0.9}Ni_{0.1}O_{2-x}$ sample are shown in Figure 1c,d, respectively. Both samples show a pre-edge peak consistent with Ni being in the $^{2+}$ oxidation state. The pre-edge peak is due to a dipole forbidden electronic transition from 1s to 3d orbitals. The number of electrons in the 3d orbitals determines the oxidation state. In 3d elements, the ligand field splitting also affects the energy of the 3d orbitals slightly. Thus, a tetrahedrally coordinated Ni^{2+} ion is slightly lower in energy than an octahedrally coordinated Ni^{2+} ion. This difference, however, is smaller than that due to a change in oxidation state, which is about 0.5 ev/1 electron change.[35,36] Therefore, we label this Ni as Ni^{2+}. The fitting of the EXAFS data yields the interatomic distances between Ni atoms and the nearest neighboring atoms (Table S2 and relevant data also shown in Figure 1e). The coordination number determined by EXAFS shows that the Ni is coordinated with 3.6 oxygen atoms and no Ni−Ni bonds were detected. The Ni−O bond length in the as-prepared sample is 1.93 Å for $Ce_{0.9}$ $Ni_{0.1}O_{2-x}$ and 2.09 Å for bulk crystalline NiO (bunsenite). The second neighbor distances were determined to be 3.08 Å for Ni−O−Ce and 2.96 Å for Ni−O−Ni.

NiO has 6 Ni−O bonds at 2.09 Å and 12 Ni−O−Ni bonds at 2.96 Å, see Tables S2 and S3. In Ni-CeO_2 there are 3.6 Ni−O bonds at 1.92 Å and 2.4 Ni−O−Ce bonds at 3.08 Å. The first shell Ni−O coordination number (3.6) is significantly different from that in NiO. The higher shell peak (Ni-O-Ce) has a significantly different bond distance from that in NiO. In XAS, scattering is proportional to the number of electrons in the scattering atom, thus Ni (28 electrons) in Ni−O−Ni is readily distinguished from Ce (58 electrons) in Ni−O−Ce. The higher shell peak indicates that all second shell atoms are Ce and not Ni. Thus, Ni−O CN, higher shell distance and the higher shell scattering atom all indicate there are no NiO clusters of any size in this sample. This is also consistent with the work of Neitzel et al.,[37] who argue based on DFT and in-situ XPS that the Ni^{2+} in the four-fold coordination is very stable against formation of NiO or metallic Ni particles.

In the fluorite structure the bond length for Ce−O is 2.34 Å (Figure 1f). The second neighbor distance for Ce−O−Ce is at 3.825 Å. For comparison, the structure of bulk NiO also is shown in Figure 1f. The EXAFS clearly shows that Ni is in an environment different from bulk NiO, it is present in a 2+ oxidation state and is present in close proximity to the Ce cations, but it is not substituting for the Ce cations. More details on the results of the EXAFS fit are presented in Table S2 (results from NSLS-II) and Table S3 (results from the Canadian Light Source). To gain further insight into the location of the Ni, and the effects of co-doping CeO_2 we analyzed the $Ce_{0.9}Ni_{0.05}Zr_{0.05}O_{2-x}$ catalyst using synchrotron high energy x-ray scattering/diffraction and XAS at the Canadian Light Source, experimental details are provided in the Supporting Information. The high energy powder x-ray diffraction pattern of $Ce_{0.9}Ni_{0.05}Zr_{0.05}O_{2-x}$ and CeO_2 is shown in Figure S3. These patterns are very similar, confirming that no secondary phases containing Ni and Zr are present, as was also concluded based on XRD analysis performed using laboratory x-ray diffraction (Figure S1). The simultaneous incorporation of Zr and Ni into the CeO_2 structure caused a small increase in the lattice constant, as seen in both the laboratory XRD data and the synchrotron XRD (Table S1).[28]

XAS analysis is presented in Figure S4 where the fits to the EXAFS region (Table S3) indicate that Ni is coordinated to four oxygen atoms. As a d^8 metal, Ni^{2+} commonly forms square planar complexes.[30] In contrast, Zr is likely coordinated to eight oxygen atoms, consistent with a cubic environment. Zr(IV) ions typically exhibit similar coordination in the ZrO_2 phase.[38] Since no new peaks corresponding to ZrO_2 are observed in the powder XRD pattern, it can be inferred that Zr(IV) is fully incorporated into the CeO_2 lattice. Additionally, the Zr−O bond distance in $Ce_{0.9}Ni_{0.05}Zr_{0.05}O_{2-x}$ is slightly longer than that in pure ZrO_2, supporting this conclusion. This elongation is expected, as the CeO_2 lattice (∼5.41 Å) is larger than that of cubic ZrO_2 (∼5.09 Å), leading to slightly longer Zr−O distances when Zr^{4+} substitutes for Ce^{4+} in CeO_2 lattice.[39]

Pair distribution function (PDF) analysis of total X-ray scattering data (Figure S5) provides further insight into the positions of Zr and Ni dopants within the CeO_2 lattice. A structural model was constructed with 90% Ce, 5% Ni, and 5% Zr occupying the same crystallographic positions (Figure 2a). Initially, the lattice parameter, atomic displacement parameters for all atoms, and crystallite size of the simulated model were refined against the experimental PDF data. To improve the fit, Ni atoms were then allowed to displace along the x [100], y [010], or z [001] directions. Based on previous reports indicating that doping of square planar d^8 metals in CeO_2 can induce oxygen vacancies, the occupancy of oxygen sites was also treated as a variable.[40]

The best-fit results revealed that Ni atoms are displaced by approximately 1.573 Å in one of the x/y/z directions relative to their original positions (Figure 2b). The local geometry around Ni is best described as distorted square planar, with Ni atoms positioned slightly away from the plane formed by the four corner oxygen atoms (Figure 2c) while the Zr(IV) ions substitute for Ce(IV) within the CeO_2 lattice. A comparison of the bond distances inferred from the PDF analysis (Figure S5) and EXAFS is shown in Table S4. The Ni−O and Ni−O−Ce bond distances obtained from the fitted PDF model closely match those from the EXAFS analysis, further supporting the conclusion that Ni^{2+} ions occupy interstitial sites, where they adopt a distorted square planar coordination environment with a Ce^{4+} ion missing from this cube of oxygen atoms. We note that the low concentration of Ni (which contributes less than 2% of the electrons in the unit cell) makes it difficult to make conclusive assignments based on PDF analysis. Our best fit is the one that is most consistent with the EXAFS analysis. Also, occupancy of Ni^{2+} in a cube of oxygen with the Ce^{4+} vacancy needs two additional positive charges to maintain charge neutrality. For a similar solid solution of Pd^{2+} in CeO_2, it has been suggested based on DFT computations that hydroxyl groups in the region of anion vacancies may help to stabilize the structure.[40]

The XRF bulk analysis of this sample shows the concentration of Ni is ∼3.4 wt % which corresponds to an overall concentration of $Ce_{0.9}Ni_{0.1}O_{2-x}$. The surface analysis of the as-prepared (calcined 500 °C in air) via XPS (survey scan Figure S6) shows a Ni concentration of 3.9 atomic % and a Ce concentration of

https://doi.org/10.1021/acscatal.6c00872
ACS Catal. 2026, 16, 10207−10221

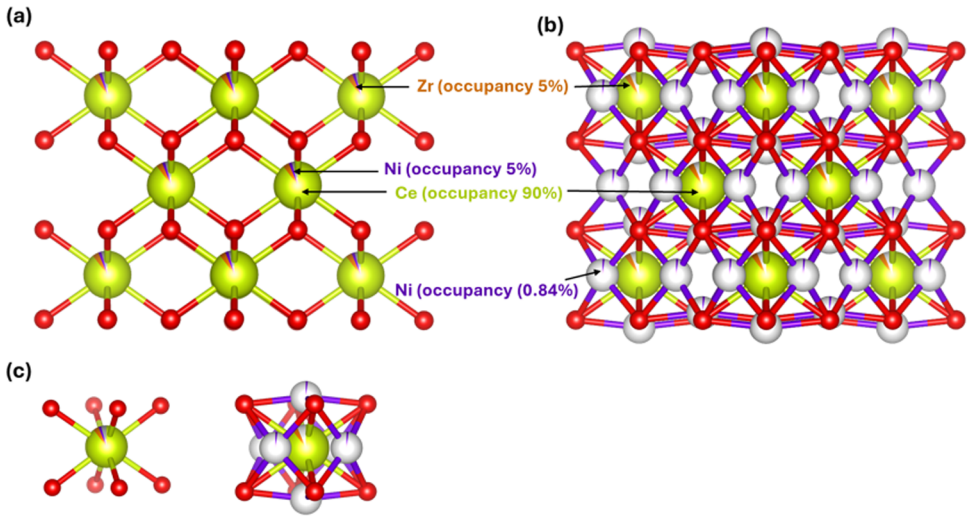

Figure 2. (a) Initial fluorite CeO_2 model used for fitting. The Zr and Ni are initially placed at the same site as Ce with a site occupancy of 5% for both Ni and Zr. (b) Best-fit model for the Ni where the atoms were allowed to move to fit the observed total x-ray scattering. The color scheme is yellow: Ce, orange: Zr, blue: Ni, red: O, and white showing the location of the Ni, with the site occupancy shown as a slice. (c) Close-up view of the coordination around a single Ce atom in the initial structure shown (a) and the relaxed structure in (b). It should be noted that the Ce atom will be missing in the cube where a Ni atom is present. The occupancy of Ni (0.84%) is based on the six possible sites, which agrees with the overall occupancy of 5%.

27.8%. The ratio of Ni/Ce (3.9/27.8 = 0.14) is slightly larger than that expected based on the bulk composition $Ni_{0.1}Ce_{0.9}O_{2-x}$ (0.1/0.9 = 0.11) suggesting that the Ni shows some surface segregation. The high-resolution scan of the Ni 2p region (Figure S7) shows a broad peak at 854.8 eV with a smaller satellite peak at 860.6 eV. This is consistent with an oxidation state of Ni^{2+} based on the literature.[41] The Ni 2p signal suggests that the ionic nickel embedded in the ceria lattice has a unique electronic structure that differs from bulk NiO. If there were NiO present in the sample, an additional peak would be expected around 856 eV,[34] which is not seen on this sample. The XPS spectrum for Ce is shown in Figure S8 and can be seen to contain 17% Ce^{3+}, which is typical for air-exposed PVP ceria samples. The O 1 s spectrum in Figure S9 shows a noticeable feature at 531.1 eV which has been assigned to oxygen vacancies or defects, but this interpretation has been questioned and instead it has also been associated with hydroxyls on the ceria.[42,43] We studied proton NMR of this sample, compared to PVP CeO_2 (Figure S10) which is consistent with this picture. However, since the peak at 531.1 eV is also seen on undoped PVP CeO_2, we have assigned it to defects in the CeO_2 associated with O vacancies.

Coordination Environment of Ni Single Atoms on the CeO_2 Surface

To understand the catalytically relevant single-site Ni in different redox environments, we propose a model in which a Ni atom is adsorbed at a step site of the CeO_2 surface. Since the EXAFS and PDF analysis show that the Ni is located in a square planar coordination within a CeO_2 cube, we would expect such structures to be located on (100) surface facets of CeO_2. However, the stable surface of CeO_2 is the (111) facet. As shown previously by Bruix et al.[44] and also in our previous work,[45] such (100) microfacets can be found on the step edges on ceria powders. Therefore we constructed a stepped surface structure from a slab comprising three O−Ce−O trilayers by selectively removing some CeO_2 units (Figure 3a), creating well-defined step edges.[46−48] As shown in Figure 3b, this modification resulted in two distinct step-edge configurations (Step-I and Step-II) that provided different coordination environments for Ni (Figure 3c,d). Our DFT calculations (details provided in Supporting Information) revealed a strong thermodynamic preference for Ni binding at the Step-II site, with adsorption energies −0.11 eV and −0.88 eV lower than the cohesive energy of Ni (−7.35 eV), for Step-I and Step-II, respectively. Under oxidizing conditions, the system undergoes an exothermic transition from NiO_2 to NiO_4 configuration through binding of two additional oxygen atoms provided by O_2 adsorption, with a large adsorption energy of −2.70 eV, indicating the stability of the square planar NiO_4 moiety on the surface. The Ni−O distances are 1.79, 1.79, 1.79, 1.86 Å, respectively, which are smaller than the EXAFS values, presumably because the latter are dominated by Ni in the bulk CeO_2 phase. The charge of the central Ni is 2+. As expected, this species is inert due to the full coordination of the Ni center, and thus inactive for catalysis.

Under reducing conditions, the NiO_4 species can be converted to NiO_3 by H_2. As shown in Figure 3g, this process starts with H_2 adsorption on the NiO_4 site (E_{ads} = −0.12 eV), followed by H−H bond cleavage with an activation barrier of 0.77 eV and reaction energy of −1.31 eV to form surface hydroxyl species. The reaction between OH and the remaining H leads to water formation (E_{act} = 0.30 eV and ΔE_r = −1.33 eV) and subsequent H_2O desorption, which is endothermic by 1.51 eV. This process, which is exothermic by 1.25 eV, is apparently responsible for the reduction peak in Figure 4a shown in the next section. In comparison, the corresponding process on CeO_2(111) is exothermic by merely 0.06 eV. The Ni in the NiO_3 site has a reduced coordination and is thus catalytically active. These results demonstrate that the oxygen coordination number of Ni can dynamically change depending on the redox environment, which in turn tunes the CO adsorption behavior as discussed below.

https://doi.org/10.1021/acscatal.6c00872
ACS Catal. 2026, 16, 10207−10221

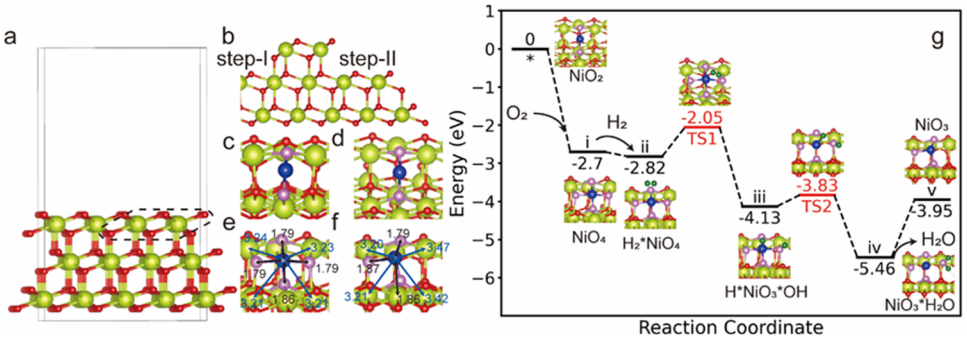

Figure 3. (a) Construction of the stepped CeO_2(111) surface model through selective removal of CeO_2 units (enclosed by dashed rectangle). (b) Resulting step-edge morphology showing two distinct coordination environments (step-I and step-II). (c, d) Optimized geometries of Ni adsorption at (c) step-I and (d) step-II sites, demonstrating different local coordinations. (e, f) Bond length analysis for Ni at the step-II site in (e) NiO_4 and (f) NiO_3 configurations, highlighting changes in Ni−O and Ni−O−Ce distances. (g) Redox-induced structural evolution between NiO_4 and NiO_3 states, showing energy profile and intermediate geometries during O_2/H_2 cycling. Color scheme: pink: O coordinated with Ni; red: O noncoordinated with Ni; yellow: Ce; teal: H; blue: Ni.

Interaction of the Catalyst with H_2 and CO

The reducibility of the Ni SAC was investigated via H_2-TPR (using 10% H_2) on the fresh catalyst and the catalyst treated up to 500 °C in H_2 was investigated by TEM to detect any phase segregation to form metallic Ni upon H_2 reduction. The total H_2 consumption can be impacted by the presence of carbonates and/or residual nitrate species which are known to adsorb on ceria, hence the as-prepared catalyst sample was first calcined at 500 °C in air to remove these species. As shown in Figure 4a, the $Ce_{0.9}Ni_{0.1}O_{2-x}$ shows two distinct reduction peaks. The first peak appears around 200 °C. This peak can be assigned to removal of O species in the vicinity of the Ni dopants in the ceria. The area of the H_2 TPR peak on the Ni SAC was quantified and shows consumption of 0.67 moles of H_2 per mole of Ni, which is consistent with the decrease in the Ni−O coordination from 3.6 to 2.5 observed by EXAFS after 200 °C H_2 treatment (Table S2). The second peak occurs around 725 °C which is assigned to removal of O from the ceria bulk. These TPR peaks are similar to those reported on pure CeO_2[49] where two reduction peaks were also seen. But in undoped ceria, the high temperature peak occurs around 800 °C due to the reduction of bulk ceria, and the low temperature peak around 400 °C which was attributed to the reduction of surface species. However, as seen in Figure 4a, the first TPR peak occurs at a much lower temperature, suggesting that the inclusion of the Ni^{2+} cations in this sample creates a defective fluorite lattice leading to more readily reducible Ce^{4+} species. Low temperature reduction features where noble metals promote ceria reduction have long been known. For example, Nunan shows ceria reduction promoted by Pt and Rh at 150 °C.[50]

A 3 wt % Ni/SiO_2 catalyst was used as a reference to illustrate the reduction of NiO into metallic Ni. This Ni/SiO_2 sample shows a prominent peak centered around 435 °C (Figure 4b), which corresponds to the conversion of nanoparticles of NiO to metallic Ni. Both of these samples were removed from the TPR system after reaching 500 °C in the H_2-TPR and imaged by TEM. The Ni/SiO_2 sample was passivated by careful exposure to pulses of oxygen to prevent deep oxidation of metallic Ni. As shown in Figure 4b, EDS mapping shows uniform dispersion of Ni indicating that it is still in the atomically dispersed form within the $Ce_{0.9}Ni_{0.1}O_{2-x}$ sample. In contrast, the Ni/SiO_2 sample shows conversion of NiO to form metallic Ni particles, as shown in Figure 4c. The TEM image shows lattice fringes corresponding to metallic Ni in the bulk, with a surface oxide that was caused by oxidation during air exposure. These results show that formation of Ni nanoparticles does not occur on the $Ce_{0.9}Ni_{0.1}O_{2-x}$ sample during H_2 treatment (in 10% H_2) at temperatures up to 500 °C.

In-situ XAS was performed on the catalyst in flowing H_2 at 200 °C and also during ethylene hydrogenation at 100 °C. There is no evidence in the XANES or EXAFS for any metallic Ni in the samples treated in the beamline (Table S2 and Figure S11a−d), which corresponds to the prominent peak seen in H_2 TPR (Figure 4a). A pre-edge feature is seen for the as-prepared sample as well as the 200 °C H_2 sample, consistent with the presence of Ni^{2+}. The first shell EXAFS peak was fit with 3.6 Ni−O bonds at 1.93 Å. After 200 °C in 10% H_2, the sample showed 2.5 Ni−O bonds with a bond distance of 1.99 A. Metallic Ni has a much shorter distance than Ni−O−Ce and much lower XANES energy. The sample also had a higher shell peak in EXAFS, which was fit with the 2.4 Ni−O−Ce bonds at 3.08 Å in the as-prepared sample. XAS scattering is proportional to the number of electrons and Ni is significantly different from Ce. Fits of the magnitude and imaginary parts of the Fourier transform clearly distinguish Ni from Ce in the second coordination shell. In addition, the bond distance of Ni−O−Ni and Ni−O−Ce are significantly different. After the H_2 treatment, the sample showed 2.1 Ni−O−Ce bonds at a distance of 2.69 Å. The drop in the number of nearest neighbor O atoms (from CN 3.6 to CN 2.5) is consistent with the TPR results (consumption of H_2 ~0.7 moles/mole of Ni) and the DFT computations (Figure 3g) being a result of the loss of neighboring O atoms.

The nature of the Ni sites was studied via DRIFTS. The $Ce_{0.9}Ni_{0.1}O_{2-x}$ sample was pretreated in O_2 at 300 °C before exposing the catalyst to flowing 10% CO, as shown in Figure 4d. The subsequent CO-DRIFTS analysis shows no peaks in the area where the nickel carbonyl bands would be observed. The sample, however, showed strong carbonate bands and a weaker broad band that would be associated with hydroxyls (Figure S12). DRIFTS however cannot provide quantitative estimates of hydroxyl density. The sample was then reduced in flowing 10% H_2 at 250 °C, followed by CO-DRIFTS. After the 250 °C treatment, well defined peaks in the carbonyl

https://doi.org/10.1021/acscatal.6c00872
ACS Catal. 2026, 16, 10207−10221

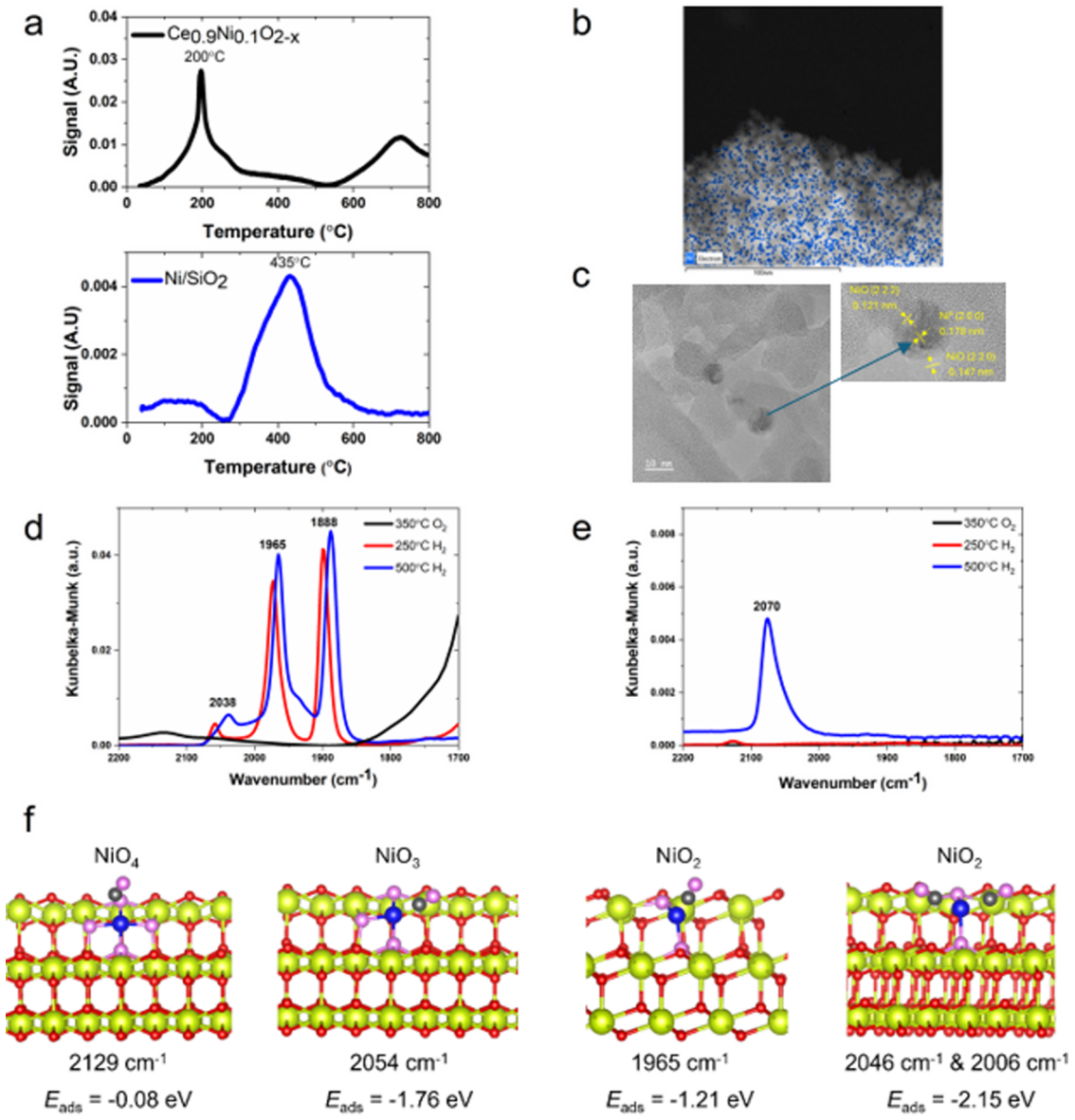

Figure 4. (a) H_2-TPR of $Ce_{0.9}Ni_{0.1}O_{2-x}$ (black) and Ni/SiO_2 (blue). (b) STEM EDS mapping of the Ni species in $Ce_{0.9}Ni_{0.1}O_{2-x}$ after a H_2-TPR treatment up to 500 °C. (c) TEM image of Ni/SiO_2 post 500 °C H_2-TPR. CO-DRIFTS spectra for (d) $Ce_{0.9}Ni_{0.1}O_{2-x}$ and (e) Ni/SiO_2. (f) Schematic depiction of vibrational modes of CO bonding to Ni in Ni/CeO_2 based on the DFT computations and corresponding wavenumber for adsorbed CO based on DFT calculations. Color scheme: pink: O coordinated with Ni and O in CO; red: O noncoordinated with Ni; yellow: Ce; blue: Ni, black: C.

region can be seen on the $Ce_{0.9}Ni_{0.1}O_{2-x}$ sample whereas the Ni/SiO_2 shows no carbonyl bands since metallic nickel has not formed by this temperature. The Ni/SiO_2 sample does show a broad hydroxyl band as seen in Figure S13.

The samples were next treated in flowing hydrogen at 500 °C followed by CO-DRIFTS. The CO adsorption peaks of the H_2-reduced Ni SAC show three features corresponding to carbonyls. None of these features were seen on the undoped ceria support (Figure S14). The three peaks are centered around 2038 cm^{-1}, 1965 cm^{-1}, and 1888 cm^{-1}. Ni/SiO_2 shows only 1 prominent band corresponding to a terminal linear CO on Ni, at 2070 cm^{-1} which is consistent with the literature.[51] The CO adsorption on the Ni doped ceria shows features that are vastly different from the results seen in literature for metallic Ni. The band centered at 2038 cm^{-1} is assigned to a terminal linear CO. The other two features that are assigned in the literature are bridged CO and multi bonded carbonyls.[51] The sample reported in Figure 4d shows strong narrow features in this region centered around 1965 cm^{-1} and 1888 cm^{-1}. The features on the Ni SAC samples stand in stark contrast to the reported DRIFTS spectra of metallic Ni (Figure 4e). The dual sharp narrow bands are commonly observed in dicarbonyl species, such as the rhodium dicarbonyl.[52]

To help assign these peaks, DFT calculations were performed to determine possible CO configurations. The possible geometry of the active sites is shown in Figure 4f, using the step model discussed above. Based on the DFT calculations, the gas phase CO exhibits a vibrational frequency of 2125 cm^{-1}. When adsorbed on NiO_4 sites, the slightly exothermic adsorption energy (−0.08 eV) and the nearly unchanged vibrational frequency (2129 cm^{-1}) indicated that a fully coordinated Ni cation bound to 4 oxygen atoms was inactive. This result was

https://doi.org/10.1021/acscatal.6c00872
ACS Catal. 2026, 16, 10207−10221

confirmed by the experimental failure in observing any carbonyl bands related to adsorbed CO on the Ni SAC sample oxidized at 350 °C (Figure 4d). DFT calculations further revealed that removal of one or two oxygen atoms from the Ni coordination sphere generates sites that are capable of CO activation. Removal of one oxygen atom (NiO_3) produces stronger CO adsorption energy of −1.76 eV and a linear terminal CO with a resulting vibrational band at 2054 cm^{-1}. With the removal of a second oxygen the Ni coordinated with 2 oxygens at the step edge or step-2O allows for the adsorption of 2 CO species. One species being the linear terminal bound CO with a resulting vibrational band at 1965 cm^{-1}. The other structure is a Ni dicarbonyl species with symmetric and asymmetric vibrational bands at 2046 cm^{-1} and 2006 cm^{1}, respectively. These computations provide an explanation for the observed CO bands on the Ni single atom catalyst.

Catalytic Reactivity for Hydrogenation Reactions

We have previously reported that the Ni doped ceria catalyst can perform acetylene hydrogenation.[30] Here we demonstrate the high selectivity of this catalyst for acetylene hydrogenation in the presence of excess ethylene. For this work, we prepared a Ni doped ceria catalyst co-doped with ZrO_2 (nominal composition $Ce_{0.9}Ni_{0.05}Zr_{0.05}O_{2-x}$ to improve thermal stability. The catalyst was tested for selective hydrogenation of acetylene in the presence of excess ethylene (C_2H_2:C_2H_4:H_2:N_2 = (1:76:4:129) with a GHSV of 32.55 ($L/g_{cat}h$)). The catalytic performance was compared with a metallic Ni/SiO_2 catalyst, which is more reactive (Figure S15a) but shows very poor selectivity due to over hydrogenation of ethylene to ethane. The bare CeO_2 and a Mg-doped CeO_2 were tested, (Figure S15b), showing no activity. The effluent composition on the Ni SAC (Figure 5a) shows that the

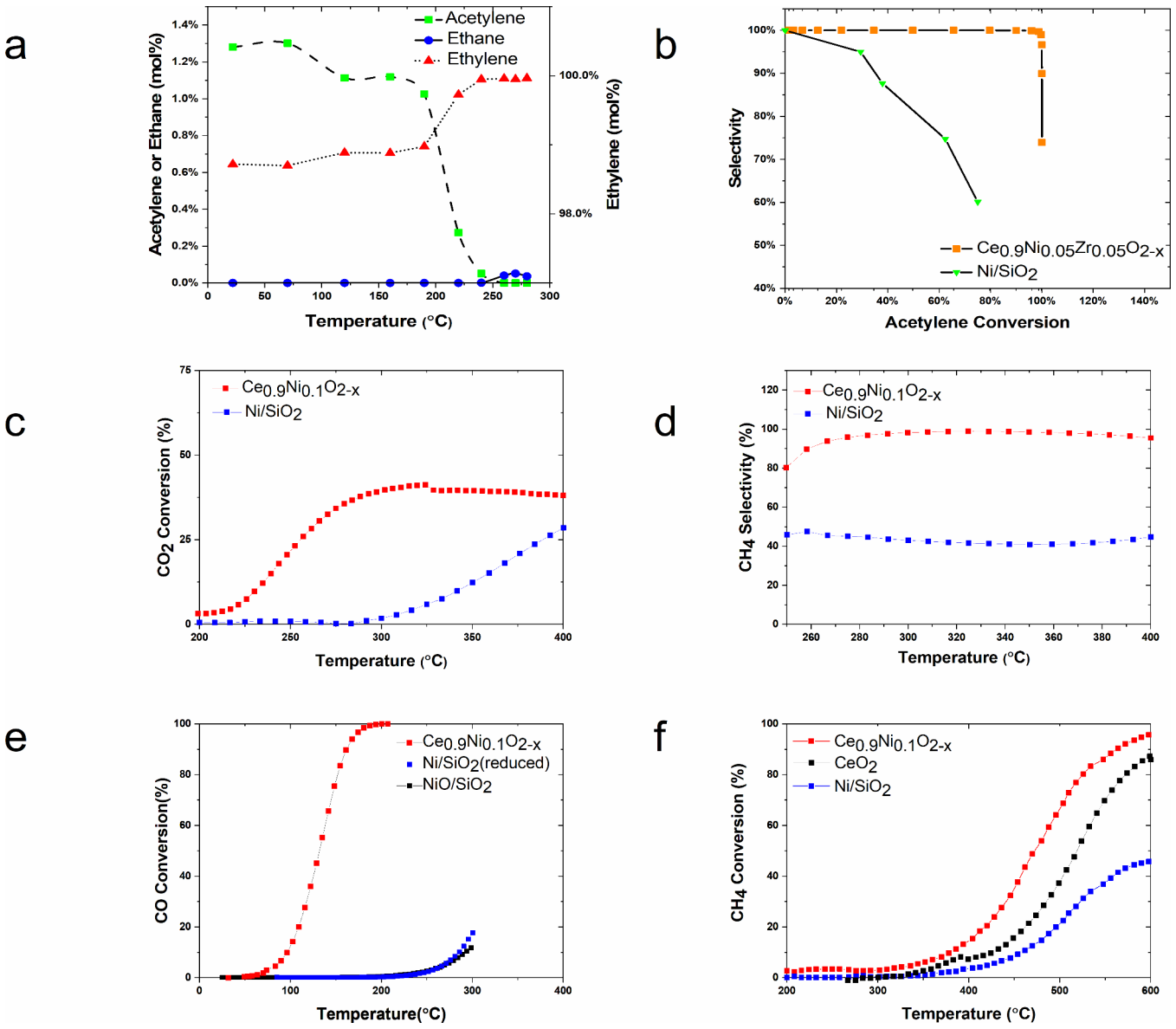

Figure 5. (a) Effluent concentrations during acetylene hydrogenation over the as-prepared $Ce_{0.9}Ni_{0.05}Zr_{.05}O_{2-x}$ catalyst. (b) Selectivity during acetylene hydrogenation over the $Ce_{0.9}Ni_{0.05}Zr_{.05}O_{2-x}$ catalyst and a metallic Ni/SiO_2. (c) Conversion for CO_2 hydrogenation over $Ce_{0.9}Ni_{0.1}O_{2-x}$ (red) and Ni/SiO_2 (blue) as a function of temperature. (d) Selectivity for CH_4 as a function of temperature during CO_2 hydrogenation. (e) CO oxidation over $Ce_{0.9}Ni_{0.1}O_{2-x}$ (red), Ni/SiO_2 with (blue) and without (black) H_2 pretreatment. (f) CH_4 oxidation over $Ce_{0.9}Ni_{0.1}O_{2-x}$ (red) and Ni/SiO_2 (blue).

https://doi.org/10.1021/acscatal.6c00872
ACS Catal. 2026, 16, 10207−10221

catalyst becomes active ~200 °C and as acetylene is consumed, we only see ethylene being produced. Only after all the acetylene is converted do we start to see ethane being produced. On the other hand, the metallic Ni catalyst becomes active at 50 °C but starts to form ethane along with ethylene (Figure S15a). Over time, the catalyst activity declines due to severe coking, and the catalyst does not achieve 100% conversion of acetylene (Figure S15a). The selectivity (moles ethylene produced per mole acetylene reacted) for both catalysts is shown in Figure 5b as a function of acetylene conversion. Metallic Ni exhibits poor selectivity due to non-selective hydrogenation to ethane. In contrast, the Ni SAC shows 100% selectivity with no formation of ethane until nearly 100% conversion of acetylene is reached.

To explore the origins of the high selectivity on the Ni SAC, we explored how the SAC can hydrogenate acetylene to form ethylene without converting any of the large excess of ethylene into ethane (Figure 5a). The experiment involved a measurement of the reactivity for ethylene hydrogenation to ethane at 75 °C. The metallic Ni/SiO_2 catalyst and the Ni SAC were tested under identical conditions, after four sets of pretreatments. The first pretreatment involved oxidation at 350 °C in air, followed by reduction in 4% H_2 at 350 °C. Both catalysts were able to achieve 100% conversion of ethylene (Figure S16a). After 30 min of ethylene hydrogenation, the catalyst was cooled and the reactor purged in inert and then used for the hydrogenation of 2% acetylene for 30 min at the reaction temperature of 75 °C. When both catalysts were subsequently tested for ethylene hydrogenation, with no additional pretreatment after the acetylene hydrogenation, we found that the deposited oligomers completely shut down the ethylene hydrogenation activity of the Ni SAC while the metallic Ni catalyst recovered quickly and was able to achieve 80% conversion in a short time. It appears that on the Ni SAC, the oligomers deposited during acetylene hydrogenation stop the hydrogenation of ethylene to ethane, while on the metallic Ni/SiO_2, these oligomers can spill over to the silica support, allowing the catalyst to continue performing ethylene hydrogenation. We have found evidence of similar spillover of coke in our previous work on propane dehydrogenation,[53] Despite significant amounts of graphitic carbon deposited on the catalyst (10 wt %), the coke is primarily located on the support, allowing the metal particles to continue being active. Following the acetylene hydrogenation, the catalysts were oxidized in air at 350 °C for 30 min. Without any further pretreatment, the Ni SAC was active for ethylene hydrogenation while the Ni/SiO_2 showed no activity since it had transformed into NiO which is not active for hydrogenation. A subsequent H_2 reduction at 350 °C restored the ethylene hydrogenation activity of both catalysts. This experiment shows that metallic Ni becomes active for hydrogenation only after a reduction in H_2 while the Ni SAC can perform hydrogenation in its oxidized state, because weakly bound oxygen atoms can be easily removed in H_2, as seen in the H_2 TPR. The Ni SAC achieves high activity around 200 °C which is the temperature where the H_2 TPR peaks are seen on this catalyst. Additional testing on the Ni/SiO_2 was done without any reduction pretreatment (Figure S16b) showing no activity during acetylene hydrogenation.

Considering the current interest in conversion of CO_2 into valuable chemical feedstocks, we explored the performance of the Ni SAC for CO_2 hydrogenation. Figure 5c,d and Figure S17a,b show a comparison of the Ni SAC with a metallic Ni/SiO_2 catalyst. During CO_2 hydrogenation, the Ni SAC catalyst showed much higher activity and was selective towards CH_4 compared with the metallic nickel (Figure 5c,d). The ionic Ni species appear to provide a direct path towards methanation,[54] whereas the metallic Ni nanoparticles catalyze the reverse water gas shift (RWGS) followed by hydrogenation of CO to CH_4. This has been elegantly demonstrated through a kinetic analysis of CO_2 hydrogenation on Ru, Co and Ni where all three metals show similar trends.[55] These authors note that there is structure sensitivity for this reaction, with smaller Ni particles favoring CO formation. The structure sensitivity has been confirmed by Simons et al.[56] who conclude that Ni nanoparticles below 5 nm in size lose their methanation activity. It is therefore not surprising that following this trend, single atom Ni catalysts would be expected to catalyze only the conversion of CO_2 to CO, as shown by Millet et al.[7] for Ni@MgO. In the context of all of this literature, it is then unusual to see high selectivity for methanation on the Ni single atom catalysts reported here (Figure 5c,d). We can explain this performance of ionic Ni from the DFT calculations and experimental measurements of Barreau et al. (ref [54]) who show that ionic Ni sites in CeO_2 can activate CO_2 by stabilizing a bent configuration where C and O can bond to neighboring Ni and Ce with a moderate adsorption energy allowing further hydrogenation to CH_4.[54] In their work, the catalyst contains domains of NiO and atomically dispersed Ni in a very similar coordination to the catalyst described here. The NiO reduces to Ni^0 under methanation conditions and was concluded largely to be a spectator. The origin of methanation activity was associated with the Ni SAC, with CN = 4 to O atoms in the ceria support.

To explore the stability of the Ni SAC for CO_2 hydrogenation, we performed long term testing at 350 °C, first for 24 h on stream, then following an oxidation, for another 16 h. As shown in Figure S17c the catalyst performance is stable, and the selectivity shown in Figure S17d of the SAC is preserved. When this catalyst was examined via TEM and STEM-EDS (Figure S17e–h) we found that ~1.15% of Ni was still atomically dispersed, the remainder had transformed into Ni nanoparticles. The reaction mixture was more reducing (37% H_2) than used previously (10%H_2) where the Ni single atom catalyst was stable against reduction (Figure 1). The results show that Ni single atoms survive at elevated temperatures under reducing conditions, but some of the Ni in the bulk gets converted to nanoparticles. The methane selectivity of this catalyst after long term testing (95% CH_4) was very different from the metallic Ni/SiO_2 catalyst (50% CH_4), suggesting that the Ni ions embedded in the ceria support were contributing significantly to the activity.

Catalytic Activity for Oxidation Reactions

We next tested these catalysts under oxidizing conditions to further distinguish the performance of the Ni SAC and metallic Ni. We found similar trends for both CO and CH_4 oxidation where the SAC vastly outperformed the metallic Ni catalyst. Traditionally, metallic Ni is known to be a poor catalyst for emission control applications such as CO oxidation. Surprisingly the Ni single site on CeO_2 allows the Ni to be active for a reaction for which Ni is not known to be a good catalyst. Previous studies[57,58] have shown that NiO particles are inactive for this reaction. Since hydrothermal stability is an important attribute for emission control catalysts. We treated the Ni SAC at 800 °C in air/10% steam for 8 h before testing for CO oxidation (Figure S18a). There was a change in the

https://doi.org/10.1021/acscatal.6c00872
ACS Catal. 2026, 16, 10207−10221

T_{50} (temperature for 50% conversion from 130 °C to 210 °C) which may be associated with the loss of BET surface area (from 151 m^2/g to 12 m^2/g). The addition of Zr co-dopant to ceria provided a modest improvement in the T_{50} of the aged catalyst. A comparison (Figure S18b) with a similar composition of a Pt based catalyst (3 wt % Pt/CeO_2) after aging at 800 °C in air/steam showed a T_{50} of 220 °C which is less active than the aged Ni SAC (210 °C) while the Ni/SiO_2 does not even make it to 50% conversion. In addition the bare CeO_2 shows no significant activity. Also, NiO has been shown to be a poor catalyst for methane oxidation.[59−61]

Since CeO_2 is known to have a high concentration of vacancies, we compared the performance of the Ni doped ceria with undoped ceria (Figure 5f). The Ni SAC presented in this work shows a T_{50} value of 446 °C which is lower than the pure ceria or the Ni/SiO_2. This is an improvement over results reported in the literature on Ni catalysts.[62] The TOF for methane oxidation on the Ni SAC is an order of magnitude greater than on Ni/SiO_2 (Figure S19a). We also tested the stability of these catalysts and found stable methane oxidation performance for the SAC, as shown in Figure S19b.

Performance of a Conventional Ni/CeO_2

In the results presented so far, we have demonstrated that Ni SAC is significantly more reactive than undoped CeO_2 or Ni nanoparticles on silica. Since CeO_2 is known to impact the performance of supported metals through metal-support interactions, we present the results of a catalyst where Ni particles are deposited on the surface of CeO_2. This catalyst was prepared via incipient wetness impregnation (IWI) on polyhedral ceria. This catalyst was tested for CO_2 hydrogenation (Figure S20a,b) and for CH_4 oxidation (Figure S20c). The results show that at similar metal loading, the performance of the IWI Ni/CeO_2 was slightly better than $Ce_{0.9}Ni_{0.1}O_{2-x}$. The selectivity of the IWI Ni/CeO_2 was comparable to $Ce_{0.9}Ni_{0.1}O_{2-x}$ with 95% selectivity to CH_4 (Figure S20b). Examination of the spent catalysts via TEM and STEM-EDS showed that the catalyst contained substantial amounts of single atom Ni species (Figure S21 and S22) in addition to Ni particles. We infer that it is difficult to prepare via impregnation a control sample which only contains metallic Ni on CeO_2. A similar observation was reported by Chen et al.[63] when 2 wt % Ni was deposited on CeO_2 nanorods and on CeO_2 prepared by the PVP sol-gel method. The most active samples for CH_4 oxidation contained very few Ni nanoparticles, with the Ni being predominantly present in atomically dispersed form. The presence of atomically dispersed Ni in IWI catalysts demonstrates the stability of single atom Ni species in a catalyst that undergoes conventional calcination (500 °C in air) and H_2 reduction (500 °C in 10% H_2), and is consistent with the computational work of Neitzel et al.[37] DFT calculations by these authors show that Ni^{2+} in the square planar site has a binding energy of 678 kJ/mole while the cohesion energy of Ni in the metal is 428 kJ/mole. The energetic driving force for converting single atoms into nanoparticles is less favorable for Ni than Pd or Pt, explaining why the Ni single atoms are so stable.

■ DISCUSSION

Preparation of single atom catalysts generally requires low metal loading to prevent formation of clusters and nanoparticles. In their work on Ni single atom catalysts,[25] Eudy et al. reported that the upper limit of Ni loading was 0.5 atom% beyond which they started to form Ni clusters. In contrast, the synthesis described here generates single atom Ni in the bulk of the ceria at a concentration of 10 atom%. The higher concentration of Ni allows us to get very good signal quality for x-ray absorption spectroscopy, helping to determine the location of the Ni ions in a distorted square planar site in the ceria lattice. The four-fold bonding geometry provides stability to the Ni^{2+} ions, consistent with the DFT computations by Figueroba and Neyman showing a binding energy 678 kJ/mol.[46] The single atom Ni survives treatment in 10% H_2 up to 500 °C, in contrast, NiO nanoparticles get converted to metallic under the same treatment conditions (Figure 4a−c). Since the catalysts were prepared by calcination in air at 500 °C, they are inherently stable under oxidizing conditions.

The XAS results show that Ni single atoms (oxidation state +2) are active for hydrogenation reactions without the need for any pre-reduction. In contrast, oxidized Ni, for example NiO or $NiAl_2O_4$ must first be converted into metallic Ni before it becomes active. And, while metallic Ni is known to be an excellent hydrogenation catalyst, it is not selective, and it is not very effective for oxidation reactions. We propose that the unusual reactivity of this Ni^{2+} in ceria is related to its square planar coordination, which is very different from the octahedral coordination in NiO, $NiTiO_3$, $NiWO_4$, La_2NiO_4, or in $NiAl_2O_4$. Indeed, square planar Ni^{2+} is rare in oxides while it is common in coordination chemistry.[64] To our knowledge, the only precedence for square planar Ni in oxides are $NdNiO_2$ and $La_4Ni_3O_8$ (made by H_2 reduction of the perovskite) and $La_3Ni_2O_6$ (made by CaH_2 reduction of the corresponding Ruddleson-Popper phase $La_4Ni_3O_{10}$).[65] However, these phases with square planar nickel also have prevalence of Ni−O−Ni linkages. The current Ni SAC materials contain square planar Ni without a Ni next-nearest neighbor. Hence, the Ni^{2+} in our Ni SAC are isolated from each other and can be considered analogous to square planar Ni^{2+} in coordination chemistry. We visualize this Ni site as 16 electron L_4Ni^{2+}, where L denotes the 2-electron donating lattice oxygen atoms. The Ni^{2+} is coordinately unsaturated and may react with nucleophiles such as CO, acetylene, ethylene, etc. to create loosely bound, 5-coordinate, 18-electron intermediates which may be active for further catalysis.

We have previously described a mechanism for C_2H_2 hydrogenation on single atom Ni sites.[66] Here we present a model for understanding why its selectivity is so much better than that of metallic Ni. We propose that the deposition of oligomers deposited during acetylene hydrogenation poison the sites that cause ethylene to be converted to ethane, as shown in Figure S16. The stronger binding of acetylene allows its hydrogenation to continue while the ethylene hydrogenation is shut down. Industrial catalysts use expensive precious metals such as palladium poisoned with silver to resist green oil formation, however even those catalysts do not promote 100% selectivity and activity can degrade over time.[57] In comparison metallic Ni sites are not selective, since they allow for deposited oligomers to be mobile so the metal site can continue to hydrogenate acetylene into ethane. A comparison of the Ni SAC with recent literature results is shown in Table S6. The Ni SAC in our work shows higher selectivity at complete conversion which exceeds the performance of other Ni based single atom catalysts reported in the literature (Table S6). However, we note a recent report of reduced Ni sites on MoS_2 based supports which provide high activity and selectivity at much lower temperatures.[67]

https://doi.org/10.1021/acscatal.6c00872
ACS Catal. 2026, 16, 10207−10221

The unique behavior of the Ni SAC during hydrogenation is further observed during CO_2 hydrogenation. It has been reported that on metallic Ni, CO_2 hydrogenation is structure sensitive leading to low selectivity towards CH_4[56,68] with decreasing particle size.[69] In this work, we observed instead high selectivity towards CH_4 (Figure 5d) in contrast to metallic Ni/SiO_2 which forms a mixture of CH_4 and CO. A comparison of the Ni SAC with reported literature on Ni catalysts is shown in Table S7. Our Ni/SiO_2 shows activity for methanation that is comparable to the literature, for example Adhikari et al.[69] report a TOF of 0.02 s^{-1} at 538 K on a range of Ni catalysts, with 10% CO_2 and 40% H_2. On our Ni/SiO_2 we find a TOF of 0.02 s^{-1} (see Supporting Information) at 533 K and 12% CO_2 and 37% H_2 while the TOF on the Ni SAC (see Supporting Information) is 0.084 s^{-1}. This higher value is comparable to the TOF reported by Xie at al.[70] after correcting for their H_2 and CO_2 partial pressures. They attributed the higher activity to sites (Frustrated Lewis Pairs, FLPs) on the ceria support and the metal-support interface. In our case, we believe that the ionic Ni in CeO_2 is responsible for the higher reactivity compared to Ni/SiO_2.

We have tested the Ni SAC for CO oxidation, in catalysts that have been hydrothermally aged at temperatures up to 800 °C in air/10% steam and determined that the atomic dispersion of the Ni is preserved. The reactivity of the Ni SAC is comparable to a similar loading of Pt/CeO_2 after the same hydrothermal aging, as shown in Figure S18. Since the Pt is all located on the surface of ceria (100% dispersion), while the Ni dispersion is estimated to be ∼19% (see TOF calculation in the Supporting Information), we estimate a higher specific reactivity for the Ni based single atom catalyst. The sol-gel synthesis used in this work is broadly applicable, as seen for a Cu SAC prepared via a similar synthesis, where it was shown that the single atom Cu sites are stable after 8 h of treatment in 10% H_2/10% steam.[71] In contrast, Cu/SiO_2 shows very low activity for CO oxidation. Table S8 shows a comparison of the Ni SAC with recent results reported in the literature where comparable performance is shown but our tests were under significantly harsher conditions (higher GHSV). The trends observed for CO oxidation were mirrored during CH_4 oxidation, where the single atom state of Ni is more active while maintaining stable performance. Table S9 shows a comparison of the Ni SAC with recent literature reports highlighting the performance during CH_4 oxidation. When the mass activity for the Ni SAC is adjusted for the 19% dispersion of the Ni (since a substantial portion of Ni is in the bulk), the Ni SAC shows excellent performance compared to the literature reports on metallic Ni catalysts. Further, CH_4 oxidation is known to be limited by water poisoning,[72] the inherent stability of the Ni single atom site shown in Figure S19 suggests resistance to water poisoning.

CONCLUSIONS

In summary, we present a versatile and robust Ni single atom catalyst that can perform oxidation as well as hydrogenation reactions without needing any pretreatment or H_2 reduction. This catalyst is versatile in terms of the wide range of reactions that can be catalyzed at rates and selectivities comparable to the benchmarks. Conventional Ni catalysts require reduction to the metallic state before they become active for hydrogenation reactions and must be protected from air exposure, otherwise they are pyrophoric. In contrast, the Ni single atom catalyst is in an oxidized state, hence can be handled in air. Furthermore, the same Ni site can catalyze oxidation and hydrogenation reactions. The unique nature of the Ni SAC can be attributed to the stabilization of Ni ions in a square planar geometry, integrated into the CeO_2 lattice. This 4-fold coordination for Ni is unusual for oxidized Ni, which is typically octahedrally coordinated to the oxygen sites. The Ni SAC is selective for methanation during CO_2 hydrogenation, shows excellent selectivity for acetylene hydrogenation in the presence of excess ethylene and can also catalyze CO oxidation and methane oxidation.

ASSOCIATED CONTENT

Supporting Information

The Supporting Information is available free of charge at https://pubs.acs.org/doi/10.1021/acscatal.6c00872.

Methods, TOF calculations, additional figures and tables (DOCX)

AUTHOR INFORMATION

Corresponding Author

Abhaya K. Datye – *Department of Chemical & Biological Engineering, University of New Mexico, Albuquerque, New Mexico 87131, United States;* orcid.org/0000-0002-7126-8659; Email: datye@unm.edu

Authors

Brandon Burnside – *Department of Chemical & Biological Engineering, University of New Mexico, Albuquerque, New Mexico 87131, United States;* orcid.org/0000-0003-2415-9916

Jesse Larence – *Department of Chemical & Biological Engineering, University of New Mexico, Albuquerque, New Mexico 87131, United States*

Ryan Alcala – *Department of Chemical & Biological Engineering, University of New Mexico, Albuquerque, New Mexico 87131, United States*

Stephen Porter – *Department of Chemical & Biological Engineering, University of New Mexico, Albuquerque, New Mexico 87131, United States;* orcid.org/0000-0002-4529-4036

Andrew DeLaRiva – *Department of Chemical & Biological Engineering, University of New Mexico, Albuquerque, New Mexico 87131, United States*

Karl Kharas – *Department of Chemical & Biological Engineering, University of New Mexico, Albuquerque, New Mexico 87131, United States*

Christopher Riley – *Department of Chemical & Biological Engineering, University of New Mexico, Albuquerque, New Mexico 87131, United States*

Angelica Benavidez – *Department of Chemical & Biological Engineering, University of New Mexico, Albuquerque, New Mexico 87131, United States;* orcid.org/0000-0001-7808-453X

Nicholas Jaegers – *Department of Chemical & Biological Engineering, University of New Mexico, Albuquerque, New Mexico 87131, United States;* orcid.org/0000-0002-9930-7672

Geunho Han – *Department of Chemical and Biological Engineering, Northwestern University, Evanston, Illinois 60208, United States*

https://doi.org/10.1021/acscatal.6c00872
ACS Catal. 2026, 16, 10207−10221

Justin Notestein – *Department of Chemical and Biological Engineering, Northwestern University, Evanston, Illinois 60208, United States*; orcid.org/0000-0003-1780-7356
Siddhant Singh – *Department of Chemistry, University of Saskatchewan, Saskatoon, Saskatchewan S7N 5C9, Canada*
Robert W.J. Scott – *Department of Chemistry, University of Saskatchewan, Saskatoon, Saskatchewan S7N 5C9, Canada*; orcid.org/0000-0003-2155-7652
Lulu Chen – *State Key Laboratory of Chemistry for NBC Hazards Protection, College of Chemistry, Fuzhou University, Fuzhou 350116, China*
Juan Li – *State Key Laboratory of Chemistry for NBC Hazards Protection, College of Chemistry, Fuzhou University, Fuzhou 350116, China*
Sen Lin – *State Key Laboratory of Chemistry for NBC Hazards Protection, College of Chemistry, Fuzhou University, Fuzhou 350116, China*; orcid.org/0000-0002-2288-5415
Hua Guo – *Department of Chemistry and Chemical Biology, Center for Computational Chemistry, University of New Mexico, Albuquerque, New Mexico 87131, United States*; orcid.org/0000-0001-9901-053X
Shan Jiang – *Davidson School of Chemical Engineering, Purdue University, West Lafayette, Indiana 47907, United States*
Wei-Ling Huang – *Davidson School of Chemical Engineering, Purdue University, West Lafayette, Indiana 47907, United States*
Jeffrey T. Miller – *Davidson School of Chemical Engineering, Purdue University, West Lafayette, Indiana 47907, United States*

Complete contact information is available at: https://pubs.acs.org/doi/10.1021/acscatal.6c00872

Author Present Address

[1]Sandia National Laboratories, Albuquerque, New Mexico 87185, United States (C.R.).

Notes

Three of the authors have a patent Single Atom Metal Doped Ceria for CO Oxidation and Hydrocarbon Hydrogenation/Oxidation (DeLaRiva et al., US 11,745,169 B1 issued Sep. 5, 2023) that was used in this research.

■ ACKNOWLEDGMENTS

Financial support for the catalyst characterization, testing, and fundamental studies was provided by the DOE Office of Science, Catalysis Science grant DE-FG0205ER15712. The EXAFS analysis was supported by the NSF/ERC CISTAR supported by the National Science Foundation under Cooperative Agreement No. EEC-1647722. A.K.D. and H.G. thank the Air Force Office of Scientific Research for generous support (Grant No. FA9550-22-1-0350). S.S. and R.W.J.S. acknowledge financial assistance from the National Sciences and Engineering Research Council (NSERC) of Canada. S.L. acknowledges the National Natural Science Foundation of China (Grants 22461160253 and 22373017) for financial support. This research used resources at the 8-ID beamline of the National Synchrotron Light Source II, a U.S. Department of Energy (DOE) Office of Science User Facility operated for the DOE Office of Science by Brookhaven National Laboratory under Contract No. DE-SC0012704. For CLS: Some of the research described in this paper was performed at the Canadian Light Source, a national research facility of the University of Saskatchewan, which is supported by the Canada Foundation for Innovation (CFI), the Natural Sciences and Engineering Research Council (NSERC), the Canadian Institutes of Health Research (CIHR), the Government of Saskatchewan, and the University of Saskatchewan.

■ REFERENCES

(1) Qiao, B.; Wang, A.; Yang, X.; Allard, L. F.; Jiang, Z.; Cui, Y.; Liu, J.; Li, J.; Zhang, T. Single-Atom Catalysis of CO Oxidation Using Pt1/FeOx. *Nat. Chem.* **2011**, *3* (8), 634–641.
(2) Liu, L.; Corma, A. Metal Catalysts for Heterogeneous Catalysis: From Single Atoms to Nanoclusters and Nanoparticles. *Chem. Rev.* **2018**, *118* (10), 4981–5079.
(3) DeRita, L.; Dai, S.; Lopez-Zepeda, K.; Pham, N.; Graham, G. W.; Pan, X.; Christopher, P. Catalyst Architecture for Stable Single Atom Dispersion Enables Site-Specific Spectroscopic and Reactivity Measurements of CO Adsorbed to Pt Atoms, Oxidized Pt Clusters, and Metallic Pt Clusters on TiO_2. *J. Am. Chem. Soc.* **2017**, *139* (40), 14150–14165.
(4) Jones, J.; Xiong, H.; DeLaRiva, A. T.; Peterson, E. J.; Pham, H.; Challa, S. R.; Qi, G.; Oh, S.; Wiebenga, M. H.; Pereira Hernández, X. I.; Wang, Y.; Datye, A. K. Thermally Stable Single-Atom Platinum-on-Ceria Catalysts via Atom Trapping. *Science* **2016**, *353* (6295), 150–154.
(5) Lu, Y.; Zhou, S.; Kuo, C.-T.; Kunwar, D.; Thompson, C.; Hoffman, A. S.; Boubnov, A.; Lin, S.; Datye, A. K.; Guo, H.; Karim, A. M. Unraveling the Intermediate Reaction Complexes and Critical Role of Support-Derived Oxygen Atoms in CO Oxidation on Single-Atom Pt/CeO2. *ACS Catal.* **2021**, *11* (14), 8701–8715.
(6) Pereira-Hernández, X. I.; DeLaRiva, A.; Muravev, V.; Kunwar, D.; Xiong, H.; Sudduth, B.; Engelhard, M.; Kovarik, L.; Hensen, E. J.; Wang, Y.; Datye, A. K. Tuning Pt-CeO2 Interactions by High-Temperature Vapor-Phase Synthesis for Improved Reducibility of Lattice Oxygen. *Nat. Commun.* **2019**, *10* (1), 1358.
(7) Millet, M.-M.; Algara-Siller, G.; Wrabetz, S.; Mazheika, A.; Girgsdies, F.; Teschner, D.; Seitz, F.; Tarasov, A.; Levchenko, S. V.; Schlögl, R.; Frei, E. Ni Single Atom Catalysts for CO2 Activation. *J. Am. Chem. Soc.* **2019**, *141* (6), 2451–2461.
(8) Tang, Y.; Wei, Y.; Wang, Z.; Zhang, S.; Li, Y.; Nguyen, L.; Li, Y.; Zhou, Y.; Shen, W.; Tao, F. F.; Hu, P. Synergy of Single-Atom Ni_1 and Ru_1 Sites on CeO_2 for Dry Reforming of CH_4. *J. Am. Chem. Soc.* **2019**, *141* (18), 7283–7293.
(9) Li, Y.; Hao, J.; Song, H.; Zhang, F.; Bai, X.; Meng, X.; Zhang, H.; Wang, S.; Hu, Y.; Ye, J. Selective Light Absorber-Assisted Single Nickel Atom Catalysts for Ambient Sunlight-Driven CO_2 Methanation. *Nat. Commun.* **2019**, *10* (1), No. 2359.
(10) Yang, H. B.; Hung, S.-F.; Liu, S.; Yuan, K.; Miao, S.; Zhang, L.; Huang, X.; Wang, H.-Y.; Cai, W.; Chen, R.; Gao, J.; Yang, X.; Chen, W.; Huang, Y.; Chen, H. M.; Li, C. M.; Zhang, T.; Liu, B. Atomically Dispersed Ni(I) as the Active Site for Electrochemical CO_2 Reduction. *Nat. Energy* **2018**, *3* (2), 140–147.
(11) Gong, Y. N.; Jiao, L.; Qian, Y.; Pan, C. Y.; Zheng, L.; Cai, X.; Liu, B.; Yu, S. H.; Jiang, H.L. Regulating the Coordination Environment of MOF-Templated Single-Atom Nickel Electrocatalysts for Boosting CO_2 Reduction. *Angew. Chem.* **2020**, *132* (7), 2727–2731.
(12) Liu, S.; Yang, H. B.; Hung, S. F.; Ding, J.; Cai, W.; Liu, L.; Gao, J.; Li, X.; Ren, X.; Kuang, Z.; Huang, Y. Elucidating the Electrocatalytic CO2 Reduction Reaction over a Model Single-Atom Nickel Catalyst. *Angew. Chem., Int. Ed.* **2020**, *59* (2), 798–803.
(13) Zhao, L.; Zhang, Y.; Huang, L.-B.; Liu, X.-Z.; Zhang, Q.-H.; He, C.; Wu, Z.-Y.; Zhang, L.-J.; Wu, J.; Yang, W.; Gu, L.; Hu, J.-S.; Wan, L.-J. Cascade Anchoring Strategy for General Mass Production of High-Loading Single-Atomic Metal-Nitrogen Catalysts. *Nat. Commun.* **2019**, *10* (1), 1278.
(14) Fei, H.; Dong, J.; Feng, Y.; Allen, C. S.; Wan, C.; Volosskiy, B.; Li, M.; Zhao, Z.; Wang, Y.; Sun, H.; An, P.; Chen, W.; Guo, Z.; Lee, C.;

Chen, D.; Shakir, I.; Liu, M.; Hu, T.; Li, Y.; Kirkland, A. I.; Duan, X.; Huang, Y. General Synthesis and Definitive Structural Identification of MN4C4 Single-Atom Catalysts with Tunable Electrocatalytic Activities. *Nat. Catal.* **2018**, *1* (1), 63–72.
(15) Li, Y.; Wu, Z.-S.; Lu, P.; Wang, X.; Liu, W.; Liu, Z.; Ma, J.; Ren, W.; Jiang, Z.; Bao, X. High-Valence Nickel Single-Atom Catalysts Coordinated to Oxygen Sites for Extraordinarily Activating Oxygen Evolution Reaction. *Adv. Sci.* **2020**, *7* (5), No. 1903089.
(16) Ohn, S.; Kim, S. Y.; Mun, S. K.; Oh, J.; Sa, Y. J.; Park, S.; Joo, S. H.; Kwon, S. J.; Park, S. Molecularly Dispersed Nickel-Containing Species on the Carbon Nitride Network as Electrocatalysts for the Oxygen Evolution Reaction. *Carbon* **2017**, *124*, 180–187.
(17) Deng, X.; Bai, R.; Chai, Y.; Hu, Z.; Guan, N.; Li, L. Homogeneous-like Alkyne Selective Hydrogenation Catalyzed by Cationic Nickel Confined in Zeolite. *CCS Chem.* **2021**, *4* (3), 949–962.
(18) Rajapaksha, R.; Samanta, P.; Quadrelli, E. A.; Canivet, J. Heterogenization of Molecular Catalysts within Porous Solids: The Case of Ni-Catalyzed Ethylene Oligomerization from Zeolites to Metal−Organic Frameworks. *Chem. Soc. Rev.* **2023**, *52* (22), 8059–8076.
(19) Chai, Y.; Wu, G.; Liu, X.; Ren, Y.; Dai, W.; Wang, C.; Xie, Z.; Guan, N.; Li, L. Acetylene-Selective Hydrogenation Catalyzed by Cationic Nickel Confined in Zeolite. *J. Am. Chem. Soc.* **2019**, *141* (25), 9920–9927.
(20) Riley, C.; Burnside, B.; Alcala, R.; Valdez, N.; Porter, S.; Huang, W.-L.; Riva, A. D. L.; Salinas, P.; Grant, R.; Rodriguez, M.; Miller, J.; Datye, A. Structurally Regenerable High Entropy Aluminate Spinel Catalysts for Dry Reforming of Methane. *ChemCatChem* **2025**, *17* (7), No. e202401949.
(21) Sahli, N.; Petit, C.; Roger, A. C.; Kiennemann, A.; Libs, S.; Bettahar, M. M. Ni Catalysts from $NiAl_2O_4$ Spinel for CO_2 Reforming of Methane. *Catal. Today* **2006**, *113* (3), 187–193.
(22) de Araujo, G. C.; de Lima, S. M.; Assaf, J. M.; Peña, M. A.; Fierro, J. L. G.; do Carmo Rangel, M. Catalytic Evaluation of Perovskite-Type Oxide $LaNi_{1-x}Ru_xO_3$ in Methane Dry Reforming. *Catal. Today* **2008**, *133*−*135*, 129–135.
(23) Khazaal, M. H.; Staniforth, J. Z.; Alfatlawi, Z. A.; Ormerod, R. M.; Darton, R. J. Enhanced Methane Reforming Activity of a Hydrothermally Synthesized Codoped Perovskite Catalyst. *Energy Fuels* **2018**, *32* (12), 12826–12832.
(24) Rogers, J. L.; Mangarella, M. C.; D' Amico, A. D.; Gallagher, J. R.; Dutzer, M. R.; Stavitski, E.; Miller, J. T.; Sievers, C. Differences in the Nature of Active Sites for Methane Dry Reforming and Methane Steam Reforming over Nickel Aluminate Catalysts. *ACS Catal.* **2016**, *6* (9), 5873–5886.
(25) Eudy, K.; Deo, S.; Weber, Z. M.; Janik, M. J.; Rioux, R. M. Dynamic Variation of Ni and Pt Single Atom Oxidation States on CeO_2 Nanocubes during CO Oxidation. *ACS Catal.* **2025**, *15* (19), 16674–16689.
(26) Li, W.; Liu, B.; Guo, Q.; Guo, W.; Zhang, S.; Qu, Y. Reaction-Induced Regioselective Reconstruction of Ni-Doped $Ce(OH)_3/CeO_2$ Enables Exceptional Activity and Selectivity for Reverse Water-Shift Reaction. *Nat. Commun.* **2025**, *16* (1), No. 7335.
(27) Cai, G.; Chin, Y.-H. Structural Dynamics and Energy Landscape of the Forward and Reverse Water−Gas Shift Catalytic Cycle on Ceria. *ACS Catal.* **2025**, *15* (24), 20342–20359.
(28) Moon, J.; Cheng, Y.; Daemen, L. L.; Li, M.; Polo-Garzon, F.; Ramirez-Cuesta, A. J.; Wu, Z. Discriminating the Role of Surface Hydride and Hydroxyl for Acetylene Semihydrogenation over Ceria through In Situ Neutron and Infrared Spectroscopy. *ACS Catal.* **2020**, *10* (9), 5278–5287.
(29) Wu, Z.; Li, M.; Overbury, S. H. On the Structure Dependence of CO Oxidation over CeO_2 Nanocrystals with Well-Defined Surface Planes. *J. Catal.* **2012**, *285* (1), 61–73.
(30) Riley, C.; De La Riva, A.; Zhou, S.; Wan, Q.; Peterson, E.; Artyushkova, K.; Farahani, M. D.; Friedrich, H. B.; Burkemper, L.; Atudorei, N.-V.; Lin, S.; Guo, H.; Datye, A. Synthesis of Nickel-Doped Ceria Catalysts for Selective Acetylene Hydrogenation. *ChemCatChem* **2019**, *11* (5), 1526–1533.
(31) Alcala, R.; DeLaRiva, A.; Peterson, E. J.; Benavidez, A.; Garcia-Vargas, C. E.; Jiang, D.; Pereira-Hernández, X. I.; Brongersma, H. H.; ter Veen, R.; Staněk, J.; Miller, J. T.; Wang, Y.; Datye, A. Atomically Dispersed Dopants for Stabilizing Ceria Surface Area. *Appl. Catal., B* **2021**, *284*, No. 119722.
(32) Wan, C.-Z., Dettling, J. C. *Aluminum-Stabilized Ceria Catalyst Compositions, and Methods of Making the Same*; US4714694A, December 22, 1987, https://patents.google.com/patent/US4714694A/en (accessed 2023-10-02).
(33) Bortun, A. ; Nunan, J. *Niobium Containing Zirconium-Cerium Based Solid Solutions*; 6605264 B2, August 12, 2003, https://patentimages.storage.googleapis.com/fa/ce/df/e36bcdf066dd26/US6605264.pdf.
(34) Gokon, N.; Suda, T.; Kodama, T. Thermochemical Reactivity of 5−15mol% Fe, Co, Ni, Mn-Doped Cerium Oxides in Two-Step Water-Splitting Cycle for Solar Hydrogen Production. *Thermochim. Acta* **2015**, *617*, 179–190.
(35) Krogman, J. P.; Gallagher, J R; Zhang, G.; Hock, A. S.; Miller, J. T.; Thomas, C. M. Assignment of the Oxidation States of Zr and Co in a Highly Reactive Heterobimetallic Zr/Co Complex Using X-Ray Absorption Spectroscopy (XANES). *Dalton Trans.* **2014**, *43* (37), 13852–13857.
(36) Zhang, G.; Yang, C.; Miller, J. T. Tetrahedral Nickel(II) Phosphosilicate Single-Site Selective Propane Dehydrogenation Catalyst. *ChemCatChem* **2018**, *10* (5), 961–964.
(37) Neitzel, A.; Figueroba, A.; Lykhach, Y.; Skála, T.; Vorokhta, M.; Tsud, N.; Mehl, S.; Ševčíková, K.; Prince, K. C.; Neyman, K. M.; Matolín, V.; Libuda, J. Atomically Dispersed Pd, Ni, and Pt Species in Ceria-Based Catalysts: Principal Differences in Stability and Reactivity. *J. Phys. Chem. C* **2016**, *120* (18), 9852–9862.
(38) Barbey, L.; Nguyen, N.; Raveau, B. Nd2BaCuO5-Type Structure: Nickel in Square Planar Coordination and Copper Mixed Valency. *J. Solid State Chem.* **1993**, *102* (1), 156–163.
(39) Fornasiero, P.; Dimonte, R.; Rao, G. R.; Kaspar, J.; Meriani, S.; Trovarelli, A.; Graziani, M. Rh-Loaded CeO2-ZrO2 Solid-Solutions as Highly Efficient Oxygen Exchangers: Dependence of the Reduction Behavior and the Oxygen Storage Capacity on the Structural-Properties. *J. Catal.* **1995**, *151* (1), 168–177.
(40) Gulyaev, R. V.; Kardash, T. Y.; Malykhin, S. E.; Stonkus, O. A.; Ivanova, A. S.; Boronin, A. I. The Local Structure of $PdxCe1_{-x}O_{2-x-\delta}$ Solid Solutions. *Phys. Chem. Chem. Phys.* **2014**, *16* (26), 13523–13539.
(41) Grosvenor, A. P.; Biesinger, M. C.; Smart, R. S. C.; McIntyre, N. S. New Interpretations of XPS Spectra of Nickel Metal and Oxides. *Surf. Sci.* **2006**, *600* (9), 1771–1779.
(42) Biesinger, M. C.; Payne, B. P.; Lau, L. W. M.; Gerson, A.; Smart, R. S. C. X-Ray Photoelectron Spectroscopic Chemical State Quantification of Mixed Nickel Metal, Oxide and Hydroxide Systems. *Surf. Interface Anal.* **2009**, *41* (4), 324–332.
(43) Morgan, D. J. Photoelectron Spectroscopy of Ceria: Reduction, Quantification and the Myth of the Vacancy Peak in XPS Analysis. *Surf. Interface Anal.* **2023**, *55* (11), 845–850.
(44) Bruix, A.; Lykhach, Y.; Matolínová, I.; Neitzel, A.; Skála, T.; Tsud, N.; Vorokhta, M.; Stetsovych, V.; Ševčíková, K.; Mysliveček, J.; Fiala, R.; Václavů, M.; Prince, K. C.; Bruyère, S.; Potin, V.; Illas, F.; Matolín, V.; Libuda, J.; Neyman, K. M. Maximum Noble-Metal Efficiency in Catalytic Materials: Atomically Dispersed Surface Platinum. *Angew. Chem., Int. Ed.* **2014**, *53* (39), 10525–10530.
(45) Kunwar, D.; Zhou, S.; DeLaRiva, A.; Peterson, E. J.; Xiong, H.; Pereira-Hernández, X. I.; Purdy, S. C.; ter Veen, R.; Brongersma, H. H.; Miller, J. T.; Hashiguchi, H.; Kovarik, L.; Lin, S.; Guo, H.; Wang, Y.; Datye, A. K. Stabilizing High Metal Loadings of Thermally Stable Platinum Single Atoms on an Industrial Catalyst Support. *ACS Catal.* **2019**, *9* (5), 3978–3990.
(46) Figueroba, A.; Kovács, G.; Bruix, A.; Neyman, K. M. Towards Stable Single-Atom Catalysts: Strong Binding of Atomically Dispersed Transition Metals on the Surface of Nanostructured Ceria. *Catal. Sci. Technol.* **2016**, *6* (18), 6806–6813.
(47) Chu, D. R.; Wang, Z. Q.; Gong, X. Q. Theoretical Insights into CO Oxidation Activities on $CeO_2(111)$ Steps. *Surf. Sci.* **2022**, *722*, No. 122096.

https://doi.org/10.1021/acscatal.6c00872
ACS Catal. 2026, 16, 10207−10221

(48) Torbrügge, S.; Cranney, M.; Reichling, M. Morphology of Step Structures on CeO_2(111). *Appl. Phys. Lett.* **2008**, *93* (7), No. 073112.
(49) Trovarelli, A. Catalytic Properties of Ceria and CeO_2-Containing Materials. *Catal. Rev.* **1996**, *38* (4), 439–520.
(50) Nunan, J. G.; Robota, H. J.; Cohn, M. J.; Bradley, S. A. Physicochemical Properties of Ce-Containing Three-Way Catalysts and the Effect of Ce on Catalyst Activity. *J. Catal.* **1992**, *133* (2), 309–324.
(51) Németh, M.; Somodi, F.; Horváth, A. Interaction between CO and a Coke-Resistant NiIn/SiO_2 Methane Dry Reforming Catalyst: A DRIFTS and CO Pulse Study. *J. Phys. Chem. C* **2019**, *123* (45), 27509–27518.
(52) Schroeder, E. K.; Finzel, J.; Christopher, P. Photolysis of Atomically Dispersed Rh/Al2O3 Catalysts: Controlling CO Coverage in Situ and Promoting Reaction Rates. *J. Phys. Chem. C* **2022**, *126* (43), 18292–18305.
(53) Alcala, R.; Dean, D. P.; Chavan, I.; Chang, C. W.; Burnside, B.; Pham, H. N.; Peterson, E.; Miller, J. T.; Datye, A. K. Strategies for Regeneration of Pt-Alloy Catalysts Supported on Silica for Propane Dehydrogenation. *Appl. Catal., A* **2023**, *658*, No. 119157.
(54) Barreau, M.; Salusso, D.; Li, J.; Zhang, J.; Borfecchia, E.; Sobczak, K.; Braglia, L.; Gallet, J.-J.; Torelli, P.; Guo, H.; Lin, S.; Zafeiratos, S. Ionic Nickel Embedded in Ceria with High Specific CO_2 Methanation Activity. *Angew. Chem., Int. Ed.* **2023**, *62* (25), No. e202302087.
(55) Hu, W.; Tate, G. L.; Iglesia, E. Mechanistic Descriptions and Kinetic Trends in CO_2 Hydrogenation on Ru, Co, and Ni Nanoparticles. *ACS Catal.* **2025**, *15* (22), 19503–19516.
(56) Simons, J. F. M.; de Heer, T. J.; van de Poll, R. C. J.; Muravev, V.; Kosinov, N.; Hensen, E. J. M. Structure Sensitivity of CO_2 Hydrogenation on Ni Revisited. *J. Am. Chem. Soc.* **2023**, *145* (37), 20289–20301.
(57) Tang, C.; Li, J.; Yao, X.; Sun, J.; Cao, Y.; Zhang, L.; Gao, F.; Deng, Y.; Dong, L. Mesoporous NiO−CeO_2 Catalysts for CO Oxidation: Nickel Content Effect and Mechanism Aspect. *Appl. Catal., A* **2015**, *494*, 77–86.
(58) Han, S. W.; Kim, D. H.; Jeong, M.-G.; Park, K. J.; Kim, Y. D. CO Oxidation Catalyzed by NiO Supported on Mesoporous Al_2O_3 at Room Temperature. *Chem. Eng. J.* **2016**, *283*, 992–998.
(59) Shu, M.; Wei, S.; Jia, C.-J.; Wang, D.-L.; Si, R. Effect of Nickel Oxide Doping to Ceria-Supported Gold Catalyst for CO Oxidation and Water-Gas Shift Reactions. *Catalysts* **2018**, *8* (12), 584.
(60) Paredes, J R; Díaz, E.; Díez, F. V.; Ordóñez, S. Combustion of Methane in Lean Mixtures over Bulk Transition-Metal Oxides: Evaluation of the Activity and Self-Deactivation. *Energy Fuels* **2009**, *23* (1), 86–93.
(61) Liu, F.; Sang, Y.; Ma, H.; Li, Z.; Gao, Z. Nickel Oxide as an Effective Catalyst for Catalytic Combustion of Methane. *J. Nat. Gas Sci. Eng.* **2017**, *41*, 1–6.
(62) Caravaggio, G.; Nossova, L.; Turnbull, M. J. Nickel-Magnesium Mixed Oxide Catalyst for Low Temperature Methane Oxidation. *Chem. Eng. J.* **2021**, *405*, No. 126862.
(63) Chen, J.; Pham, H. N.; Mon, T.; Toops, T. J.; Datye, A. K.; Li, Z.; Kyriakidou, E. A. Ni/CeO_2 Nanocatalysts with Optimized CeO_2 Support Morphologies for CH_4 Oxidation. *ACS Appl. Nano Mater.* **2023**, *6* (6), 4544–4553.
(64) Cotton, F.A.; Wilkinson, G.; Murillo, C. A.; Bochmann, M. *Advanced inorganic chemistry*; John Wiley & Sons, **1999**. https://chemistlibrary.wordpress.com/wp-content/uploads/2015/05/cotton-wilkinson-advanced-inorganic-chemistry.pdf (accessed 2026-03-31).
(65) Poltavets, V. V.; Lokshin, K. A.; Dikmen, S.; Croft, M.; Egami, T.; Greenblatt, M. $La_3Ni_2O_6$: A New Double T′-Type Nickelate with Infinite $Ni^{1+/2+}O_2$ Layers. *J. Am. Chem. Soc.* **2006**, *128* (28), 9050–9051.
(66) Riley, C.; Zhou, S.; Kunwar, D.; Payne, R.; Gao, L.; Lin, S.; Guo, H.; Datye, A. Design of Effective Catalysts for Selective Alkyne Hydrogenation by Doping of Ceria with a Single-Atom Promotor. *J. Am. Chem. Soc.* **2018**, *140* (40), 12964–12973.
(67) Liu, Y.; Yang, N.; Feng, H.; Li, N.; Zhang, X.; Sheng, Z.; Lv, Y.; Dai, S.; Tian, S.; Li, D. Engineering Heterogeneous Dual-Coordination Environments for Single-Atom Nickel Catalysts: A Synergistic Strategy to Enhance Selective Hydrogenation. *J. Am. Chem. Soc.* **2025**, *147* (50), 45966–45976.
(68) Schmider, D.; Maier, L.; Deutschmann, O. Reaction Kinetics of CO and CO_2 Methanation over Nickel. *Ind. Eng. Chem. Res.* **2021**, *60* (16), 5792–5805.
(69) Adhikari, D.; Whitcomb, C. A.; Zhang, W.; Zhang, S.; Davis, R. J. Revisiting the Influence of Ni Particle Size on the Hydrogenation of CO_2 to CH_4 over Ni/CeO_2. *J. Catal.* **2024**, *438*, 115708.
(70) Xie, Y.; Chen, J.; Wu, X.; Wen, J.; Zhao, R.; Li, Z.; Tian, G.; Zhang, Q.; Ning, P.; Hao, J. Frustrated Lewis Pairs Boosting Low-Temperature CO_2 Methanation Performance over Ni/CeO_2 Nanocatalysts. *ACS Catal.* **2022**, *12* (17), 10587–10602.
(71) Larence, J.; Pham, H.; De, A.; Riva, L.; Alcala, R.; Burnside, B.; Bujanda, E.; Benavidez, A.; Dagle, V.; Wang, H.; Moskowitz, B. M.; Affandy, M.; Dagle, R.; Huang, W.-L.; Jiang, S.; Kim, T.; Miller, J.; Datye, A. *Hydrothermally Stable Single Atom Cu Catalysts on CeO2*; March 25, 2026.
(72) Li, X.; Wang, X.; Roy, K.; van Bokhoven, J. A.; Artiglia, L. Role of Water on the Structure of Palladium for Complete Oxidation of Methane. *ACS Catal.* **2020**, *10* (10), 5783–5792.

https://doi.org/10.1021/acscatal.6c00872
ACS Catal. 2026, 16, 10207−10221